NUMERICAL AND EXPERIMENTAL INVESTIGATION OF THERMAL PERFORMANCE OF GRAPHENE REINFORCED ALUMINIUM

A Thesis Submitted to
the Graduate School of
İzmir Institute of Technology
in Partial Fulfillment of the Requirements for the Degree of

MASTER OF SCIENCE

in Energy Engineering

by
Ahmet Berk YILMAZ

December 2020
İZMİR

ACKNOWLEDGMENTS

Firstly, I would like to thank my supervisor Assist. Prof. Dr. Kasım Toprak for his advices and support during my research. I also thank my co-supervisor Assoc. Prof. Dr. Sinan Kandemir for his support.

I would like to thank The Scientific and Technological Research Council of Turkey (TUBITAK) for their financial support. This work is partially supported by TUBITAK (Grant No: 116F115).

The numerical calculations reported in this thesis were performed at TUBITAK ULAKBIM, High Performance and Grid Computing Center (TRUBA resources).

I also thank my friends Serkan Erol and Ali Arıdıcı from Fluid Dynamics Laboratory for their help and advices.

I am very grateful to my father İrfan Yılmaz, my mother Nuran Yılmaz and my little sister Miray Yılmaz for their love, support and good wishes they've given me all the time. I would also like to extend my gratitude to my dearest girlfriend Pelin Çiçek Engin for her love and support.

ABSTRACT

NUMERICAL AND EXPERIMENTAL INVESTIGATION OF THERMAL PERFORMANCE OF GRAPHENE REINFORCED ALUMINIUM

Graphene is a material with superior properties such as high thermal conductivity and mechanical strength. These exceptional properties make graphene a good candidate for being used as a reinforcement agent in other materials. Aluminium is a widely used material in industry for thermal applications for being cheap, lightweight and having high thermal conductivity. In the literature, there are many examples of graphene reinforced aluminium production. Also, the effects of graphene on thermal conductivity and mechanical properties of aluminium are also investigated experimentally. However, there are limited molecular dynamics studies for graphene-aluminium composites.

In this work, aluminium, graphene and graphene coated aluminium are modeled and simulated with non-equilibrium molecular dynamics method. Length, width, height, temperature dependence of thermal conductivity of these models are investigated. In addition, the effects of graphene layer number, defect orientation, defect size and defect location are also reported.

Additionally, an experimental setup is designed and produced for a comparative thermal performance study. Thermal performances of aluminium alloy and graphene nanoplatelet reinforced aluminium are investigated with a convection heat transfer test.

ÖZET

GRAFEN TAKVİYELİ ALÜMİNYUMUN TERMAL PERFORMANSININ SAYISAL VE DENEYSEL OLARAK İNCELENMESİ

Grafen yüksek termal iletkenlik ve mukavemet gibi üstün özelliklere sahip bir malzemedir. Bu istisnai özellikleri, grafeni, diğer malzemelerin özelliklerinin güçlendirilmesinde kullanılması için iyi bir aday yapmaktadır. Alüminyum, ucuz, hafif, dayanıklı ve yüksek termal iletkenliğe sahip olmasından dolayı sanayide oldukça fazla kullanılan bir malzemedir. Literatüde, grafen ile güçlendirilmiş alüminyum üretiminin çeşitli örnekleri bulunmaktadır. Ayrıca literatürde, grafenin alüminyumun termal iletkenliğine ve mekanik özelliklerine olan etkisinin deneysel olarak incelendiği çalışmalar da bulunmaktadır. Fakat, grafen-alüminyum kompozitleri için yapılmış çok az sayıda moleküler dinamik çalışması bulunmaktadır.

Bu çalışmada, saf alüminyum, grafen ve grafen kaplı alüminyum modellendi ve moleküler dinamik yöntemi ile simüle edildi. Uzunluk, genişlik, kalınlık ve sistem sıcaklığı gibi parametrelerin bu modellerin termal iletkenliği üzerindeki etkisi incelendi. Ayrıca, grafen katman sayısı, hata boyutu, hata şekli ve hata konumunun etkisi de hesaplandı.

Ek olarak, karşılaştırmalı bir çalışma için deney düzeneği tasarlandı ve üretildi. Konveksiyon yoluyla ısı transferi testi grafen ile güçlendirilmiş alüminyum ve saf alüminyum malzemeler üzerinde yapıldı ve grafenin termal performansa etkisi bu yöntemle incelendi.

TABLE OF CONTENTS

LIST OF FIGURES vii

LIST OF TABLES ix

LIST OF SYMBOLS x

CHAPTER 1 INTRODUCTION 1

1.1. Graphene 1

1.2. Experimental Investigations on Graphene Reinforced Composites 3

1.3. Numerical Investigations of Graphene and Graphene Reinforced Composites 4

1.4. Motivation of the Study 6

CHAPTER 2 MOLECULAR DYNAMICS 7

2.1. Nonequilibrium Molecular Dynamics Simulation 7

2.2. Calculation of Thermal Conductivity 8

2.2.1. Creating Atomistic Structures 9

2.2.2. Interatomic Potentials 10

2.2.3. Thermostat 16

2.2.4. Massage Passing Interface 17

2.2.5. Time Integration 18

2.2.6. Calculation of Temperature 19

CHAPTER 3 MATERIALS & METHODS 22

3.1. Numerical Modelling 22

3.1.1. Atomistic Structures 22

3.1.2. Code Structure 26

3.2. Experimental Setup 27

3.2.1. Sample Production 29

3.2.2. Sample Holder Design 30

3.2.3. Methodology 31

CHAPTER 4 RESULTS 34

4.1. Numerical Results 34

4.1.1. Pure Aluminium 34

4.1.2. Graphene 36
4.1.3. Graphene Coated Aluminium 39
4.1.4. Defected Graphene 40
4.1.5. Defected Graphene Coated Aluminium 43
4.2. Experimental Results 45

CHAPTER 5 CONCLUSION 47

APPENDIX A TECHNICAL DRAWINGS OF SAMPLE HOLDER 50

APPENDIX B C++ ALGORITHMS FOR INTERATOMIC POTENTIALS 52

APPENDIX C FAN CHARACTERISTICS 57

REFERENCES 58

LIST OF FIGURES

Figure **Page**

Figure 1.1 Allotropes of carbon atom 1
Figure 2.1 A representative schematic of an NEMD simulation domain 8
Figure 2.2 Representative scheme of the alignment of graphene and metal structure 9
Figure 2.3 An example of part of a structure file for a simulation 9
Figure 2.4 Representative schematic of a sample region divided into 8 equal slabs 10
Figure 2.5 A typical graph of Lennard-Jones interatomic potential 12
Figure 2.6 Temperature change along simulation time for two different τ values 17
Figure 2.7 An example of the temperature distribution across a model 20
Figure 3.1 Molecular structures of the models used for simulations 23
Figure 3.2 Representative schematic of the graphene coated aluminium model 23
Figure 3.3 Atomistic structures of defected models 24
Figure 3.4 Interatomic potentials for simulations 25
Figure 3.5 Structure of the NEMD code 26
Figure 3.6 Detailed side view of atomistic structure of graphene coated aluminium model 27
Figure 3.7 Schematic representation of the experimental setup 28
Figure 3.8 Al360 and GNR reinforced Al samples 29
Figure 3.9 SEM image of Al360/0.5wt.% GNP composite (Martin, Kandemir, and Antonov 2020) 29
Figure 3.10 3D model of bottom part of the sample holder 30
Figure 3.11 3D model of the upper part of the sample holder 30
Figure 3.12 3D models of the sample holder: a) bottom part b) final assembly 31
Figure 3.13 Schematic of thermocouple placements in the sample holder 32
Figure 3.14 Steady-state temperature distribution for the Gr-Al sample 32
Figure 3.15 Picture of the experimental setup 33
Figure 3.16 Zoom-in pictures of the experimental setup a) control units, b) sample holder 33
Figure 4.1 Length effect of thermal conductivity of pure aluminium 35
Figure 4.2 Height (a) and width (b) effect on thermal conductivity of pure aluminium 35

Figure **Page**

Figure 4.3 The comparison of the thermal conductivity results with reference work for SLG 36
Figure 4.4 Length effect on thermal conductivity of suspended graphene 37
Figure 4.5 Temperature gradient across 200 Å suspended graphene layer 37
Figure 4.6 Temperature effect on thermal conductivity of SLG 38
Figure 4.7 Length effect of thermal conductivity for aluminium, SLG coated aluminium and BLG coated aluminium 39
Figure 4.8 Graphene layer number effect on the thermal conductivity of 60 Å long aluminium 40
Figure 4.9 Effect of point defect density on thermal conductivity for SLG 41
Figure 4.10 Effect of defect orientation and length on thermal conductivity of SLG 42
Figure 4.11 Comparison of thermal conductivities among SLG with different defect shapes 43
Figure 4.12 Thermal conductivity with increasing density of point vacancies on graphene coated aluminium 44
Figure 4.13 Defect orientation and length effects on thermal conductivity for graphene-coated aluminium 45
Figure 4.14 Air speed vs. inlet-outlet temperature difference for comparison of 0.5wt.%GNP reinforced and non-reinforced Al samples 46
Figure A.1 Technical drawing of bottom part of the sample holder 50
Figure A.2 Technical drawing of upper part of the sample holder 51
Figure C.1 Fan voltage vs. outlet air speed and Reynolds number 57

LIST OF TABLES

Table **Page**

Table 1.1 List of properties for single layer graphene 2
Table 2.1 Q-SC parameters for some metals (Kimura et al. 1998) 14
Table 2.2 Tersoff Potential parameters for C-C bonding interactions 16
Table 3.1 Common structure dimensions for all simulations 25

LIST OF SYMBOLS

SYMBOLS

κ	thermal conductivity
m	mass
r	distance between atoms
f	force
t	time
U	potential energy
ε	bonding energy
v	velocity
a	acceleration
T	temperature
τ	damping constant
k_b	Boltzmann Coefficient
N	number of atoms
L	length
E	energy

INDICES

ph	phonon
e	electron
c	cut-off
g	gap
sr	source
sn	sink
in	inlet
out	outlet
kin	kinetic

CHAPTER 1

INTRODUCTION

Advanced materials are being developed for meeting the needs of developing technology. Fast heat dissipation is one of these needs in many industries. For example, in electronics, heat dissipation is crucial for increasing the lifetime and performance of devices. Graphene is one of these advanced materials that has high thermal conductivity. This section includes the explanation of graphene, some of the applications of graphene and experimental and numerical studies from the literature.

1.1. Graphene

Carbon has several allotropes and graphene is one of the allotropes of a Carbon atom. Diamond, Graphite, Lonsdaleite, Fullerene and Carbon Nanotube (CNT) are other most known allotropes of Carbon. Molecular structures of these allotropes are shown in Figure 1.1. These allotropes are named diamond, graphite, lonsdaleite, fullerene C-60, fullerite C-540, fullerene C-60, amorphous carbon, carbon nanotube, respectively.

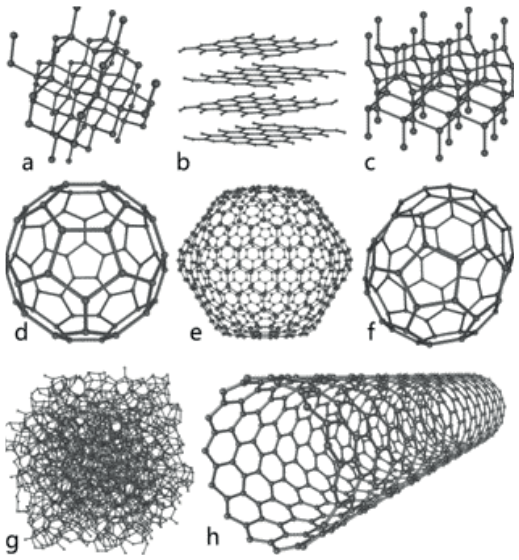

Figure 1.1 Allotropes of carbon atom

Graphene is a single layer, carbon-based material with a honeycomb-shaped lattice structure. In 2004, Andre Geim and Konstantin Novoselov had produced the first graphene layer from graphite (Novoselov et al. 2005). After this invention, several researches have been made for investigating the properties of graphene. It was found that graphene has extraordinary properties. For example, Balandin et al. (Balandin et al. 2008) investigated the thermal conductivity of suspended graphene sheet experimentally and found that graphene has superior thermal conductivity around 4840-5300 W/mK. This shows that graphene has higher thermal conductivity than CNTs and other advanced materials. In another research, Lee at al. (Lee et al. 2008a) investigated the mechanical properties of graphene and obtained that graphene has 1000 GPa of Young Modulus which makes it the strongest material ever measured. Besides the superior mechanical and thermal properties of graphene, it is also discovered that graphene is also a good corrosion barrier for liquid applications when it is coated on copper or aluminium (Kousalya et al. 2013; Jianhua Liu et al. 2015). Table 1.1 shows the properties of single-layer graphene from the literature.

Table 1.1 List of properties for single layer graphene

Property	Value	References
Young's modulus	1.0 TPa	(Lee et al. 2008b)
Fracture strength	130 GPa	
Tensile Strength	100 GPa	
Thermal conductivity	5000 W/mK	(Balandin et al. 2008)
Shear modulus	280 GPa	(X. Liu et al. 2012)
Longitudinal sound velocity	20 km/s	(Baimova et al. 2013)
Melting temperature	4900 K	
Optical transmittance	97.70%	(Edwards and Coleman 2013)
Electron mobility	250.000 cm^2/Vs	(Bolotin et al. 2008)

These studies showed that graphene can be used as a reinforcing material for many applications in various fields such as automotive, space, and electronics. Aluminium is widely used in electronics, aerospace, and automotive industries. It is lightweight and cheap. Moreover, it has high thermal conductivity and low thermal coefficient of expansion (Han et al. 2018). These features of graphene and aluminium created a new

area for aluminium-graphene composite researches. In the further sections, numerical and experimental studies of graphene-metal composites from the literature will be given.

1.2. Experimental Investigations on Graphene Reinforced Composites

Graphene is a potential reinforcing agent to enhance the properties of existing materials due to its superior features. In the literature, there are many examples of graphene-polymer, graphene-metal and graphene-ceramic composites (Porwal, Grasso, and Reece 2013; Mohan et al. 2018). Experimental studies have been made for investigating the performance of graphene-enhanced materials for different purposes. In one of these studies, the thermal performance of graphene-coated aluminium and an uncoated aluminium box filled with PCM is investigated. It was found that graphene-coated aluminium box absorbs more heat and it reaches 105°C of maximum temperature in 80 minutes where uncoated one reaches 77°C degrees of maximum temperature in 30 minutes (Abhinav et al. 2017). In another study, Cho et al. (Cho et al. 2017) found that graphene coating increases the heat dissipation for LED applications which leads to increasing the performance and the lifetime of the LED. Zhang et al. (Y. F. Zhang et al. 2016) reported a thermal enhancement of 3329% in thermal conductivity of a polymer reinforced with vertically aligned graphene particles. Fang et al. (Fang et al. 2013) investigated the graphene-PCM (Phase Change Materials) composites and showed that 400% enhancement can be achieved in thermal conductivity of PCM with 10 wt.% graphene loading. Kuang et al. (Kuang et al. 2013) presented a 15% improvement in thermal conductivity of graphene-based Ni composites comparing to pure Ni. In another study, Gao et al. (Sharma, Kumar, and Chandra 2017) investigated 10% increment in thermal conductivity when a copper matrix is reinforced with graphene. These researches showed that graphene can enhance the thermal properties of different materials in different scales. Other than the materials mentioned above, aluminium, being one of the most utilized materials in the industry, has gained great attraction for aluminium-graphene composite related researches.

Many attempts have been done for producing graphene reinforced aluminium metal matrix composites (AMMCs). For instance, graphene reinforced AMMCs have been produced with friction stir processing (FSP) (Jeon et al. 2014), powder synthesis (Yan et al. 2014; Jinghang Liu et al. 2016; Shin et al. 2015), vacuum hot pressing (Huang

et al. 2016) and chemical vapour decomposition (CVD) methods (Zheng et al. 2016). Experimental studies show that graphene helps to increase both the thermal conductivity and the strength of the aluminium (Han et al. 2018). Also, Zheng et al. showed that graphene surface can successfully be achieved on the aluminium surface and this increases the anticorrosion properties of aluminium (Zheng et al. 2016). Among these studies, many others investigated the thermal conductivity of graphene-aluminium composites. Jeon et al. (Jeon et al. 2014) found that graphene reinforced AMMC fabricated by FSP has 15% higher thermal conductivity than pure aluminium. Another research showed that 15.4% enhancement in thermal conductivity can be achieved by adding graphene into pure Al by powder metallurgy technique (L. Zhang et al. 2018). Moreover, Saboori et al. (Saboori et al. 2017) observed that the fabrication process of graphene-aluminium composites affects the thermal conductivity. Composite produced by press-sintering process has 5% more thermal conductivity than that of the hot-rolled composite. In the literature, there are also application-based researches for graphene-metal composites. For instance, Cho et al. (Cho et al. 2017) compared the thermal performance of Cu and Graphene-Cu based heat sinks for an LED. Abhinav et al. (Abhinav et al. 2017) investigated the graphene-coated aluminium box for thermal energy storage applications. Furthermore, Hsieh et al. (Hsieh et al. 2017) used a microwave-assisted method to produce graphene nanosheets on a Cu surface to investigate thermal transport enhancement for heat sink applications. These researches show that graphene can play a vital role in thermal management and energy storage applications in the future.

1.3. Numerical Investigations of Graphene and Graphene Reinforced Composites

Since it is difficult and expensive to investigate the properties of nano-scale materials experimentally, numerical methods such as molecular dynamics (MD) simulations are preferred for graphene researches. In this chapter, some of the MD studies for graphene, aluminium and graphene coating of metals from the literature will be given.

Besides the experimental studies, the MD simulation technique is also a widely used method that is used in materials science. In the literature, many studies are investigating the dependence of thermal conductivity of graphene on parameters such as

length, width, edge shape, temperature. Su and Zhang (Su and Zhang 2018) calculated the length and width dependence of the phonon thermal conductivity (κ_{ph}) of suspended and supported graphene. It was shown that κ_{ph} of graphene increases as the length and width increases. Besides, κ_{ph} of graphene decreases when it is supported by Si substrate. In another study, the change of κ_{ph} of graphene with three different interatomic potentials (Optimized Tersoff, Brenner and Original Tersoff) was studied (Cao 2012). Significant enhancement was found in κ_{ph} of graphene (up to 2500 W/mK) with Optimized Tersoff potential. The effect of temperature to the κ_{ph} was also calculated and it was found that κ_{ph} increases from 100 to 300 K and decreases from 300 K to 1000 K (Cao 2012). κ_{ph} of multilayer graphene was also investigated and the results showed that the κ_{ph} decreases due to the restriction of vibration of carbon atoms by other layers as the number of graphene layers increases (Wei et al. 2011).

Different types of defects may occur on a graphene sheet during the production stage. These defects affect the chemical and mechanical properties of materials. It is important to understand the properties of graphene under defective circumstances to use it for practical applications. For this reason, MD methods are used widely to understand the impact of defects on the thermal conductivity of graphene. For example, the effects of different type of defects on the thermal conductivity of graphene was investigated (Mortazavi and Ahzi 2013). It was reported that as the concentration of defects increase the thermal conductivity decreases and converges. Thermal conductivity decrement trend for all defect types (point vacancy defects, bi-vacancy defects, Stone-Wales defects) were similar and a significant reduction was observed at 0.25% concentration ratio. It was also reported that 2% concentration of bi-vacancy and point defects results in elastic modulus to decrease by 20%. In another study, room temperature thermal conductivity was tested for parallel and vertical defect orientations. It was reported that parallel defects affect thermal conductivity 50% less than the vertical case. So, the thermal conductivity is strongly dependent on the defect orientation (Rajabpour and Vaez Allaei 2012). Moreover, Feng et al. reported that Stone-Wales defect affects the thermal conductivity of SLG less than point vacancy for same defect concentrations (90% and 95% reduction respectively) (Feng et al. 2015). In another study, it was reported that increasing projected area of the defect morphology perpendicular to the heat flow direction reduces the thermal conductivity more. Reduction in thermal conductivity is in the order of vertical, circular and horizontal from higher to lower (Zhan et al. 2018). Zhang et al. also showed that the

thermal conductivity of graphene is highly dependent on the defect density in low concentrations (Y. Y. Zhang et al. 2012).

In the literature, there are MD studies for aluminium and graphene-coated metals for investigation of κ_{ph} of these materials. Starting from the aluminium, κ_{ph} was investigated in several studies (Wang, Lu, and Ruan 2016; Ya Zhou, Anglin, and Strachan 2007; Chantrenne, Raynaud, and Barrat 2003; Jain and McGaughey 2016). Wang et al. (Wang, Lu, and Ruan 2016) presented a density functional theory (DFT) study for thermal conductivity of aluminium at room temperature. It was found that the κ_{ph} of Al is around 5.8 W/mK. Zhou et al. (Ya Zhou, Anglin, and Strachan 2007) presented an NEMD study and found κ_{ph} for Al at 300 K of 20.6 W/mK. Another NEMD study was done by Chantrenne et al. (Chantrenne, Raynaud, and Barrat 2003) and Jain et al. (Jain and McGaughey 2016) and the κ_{ph} of Al was found around 6 W/mK in both studies.

In the literature, there are several studies investigating graphene-coated metal composites with MD method (Sharma, Kumar, and Chandra 2017; Sharma et al. 2018; Erturk, Kirca, and Kirkayak 2018; Lei, Yan, and Lv 2019; Yu Zhou et al. 2019). However, all these studies focused on the mechanical properties of these materials. For instance, Sharma et al. (Sharma, Kumar, and Chandra 2017; Sharma et al. 2018) performed MD analysis for graphene-copper and graphene- nickel composites concluding that graphene increases the thermal conductivity and the Young Modulus of copper and nickel. Erturk et al. (Erturk, Kirca, and Kirkayak 2018) reported 88% enhancement in Young Modulus of pure aluminium by graphene coating.

1.4. Motivation of the Study

As mentioned in Section 1.2 and Section 1.3, the effect of graphene on the thermal conductivity of aluminium has not been studied yet. Hence, in the literature, there is a lack of thermal conductivity studies for graphene-aluminium composites. Being motivated from this, the thermal conductivity of graphene, aluminium, graphene-coated aluminium and effects of parameters such as length, height, width, temperature, layer number, defect size, defect shape and defect orientation are investigated in this thesis. Also, part of this thesis has been prepared as part of a TUBITAK (Scientific and Technological Research Council of Turkey) project (Grant No: 116F115).

CHAPTER 2

MOLECULAR DYNAMICS

MD is a frequently used technique for having a better understanding of behaviour of atoms. MD is used in many fields such as theoretical physics, biochemistry, biophysics and materials science. In materials science, MD is mostly used for investigating chemical, electrical, mechanical and thermal properties of materials. In this chapter, the basics of MD technique such as interatomic potentials, time integration and calculation of thermal conductivity of a model are explained in detail.

2.1. Nonequilibrium Molecular Dynamics Simulation

The data collected from MD simulations can be used to calculate thermal, physical and chemical properties of materials. Thermal conductivity is one of these properties which represents the ability of a material to transfer heat. Thermal conductivity can be calculated by using velocity information of each particle in the system. Heat transfer in solid materials is called conduction. Conduction takes place with two mechanisms: By phonons and electrons. Phonons are described as vibrational motions of atom groups. If a rectangular cross-shaped aluminium bar is heated from one side, the aluminium atoms which are close to the heat source will gain energy and start to vibrate faster. This will affect other atoms in the aluminium structure and heat will be transferred from one side to other. This phenomenon is called phonon heat transfer. Electrons are the other mechanism of heat conduction in metals and heat transfer along metals is dominated by electron heat transfer. Total thermal conductivity of a metal is equal to the sum of electron thermal conductivity (κ_e) and phonon thermal conductivity (κ_{ph}).

$$\kappa_t = \kappa_{ph} + \kappa_e \tag{2.1}$$

Classical MD technique only calculates the trajectory of the nuclei of atoms in a molecular structure but not the movement of electrons. Therefore, the thermal

conductivity that is calculated with a classical MD simulation includes only the phonon thermal conductivity. Two widely used approaches to calculate κ_{ph}: Equilibrium Molecular Dynamics (EMD) and Non-Equilibrium Molecular Dynamics (NEMD) simulations. κ_{ph} calculation with EMD simulation is based on Green-Kubo relation where NEMD simulation uses the Fourier's law of thermal conduction (Matsubara et al. 2016).

2.2. Calculation of Thermal Conductivity

In the NEMD simulation, the main idea is creating a temperature profile across the model by applying hot (heat source) and cold (heat sink) thermostats on two opposite sides of the model. Figure 2.1 shows the typical simulation domain for NEMD technique. Here, as the energy flows from the heat source to the heat sink, it creates a temperature gradient.

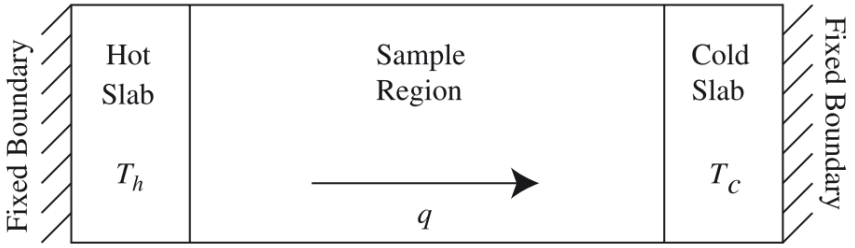

Figure 2.1 A representative schematic of an NEMD simulation domain

In this project, the NEMD code is written on C++ language with Massage Passing Interface (MPI). The numerical calculations reported in this paper were partially performed at TUBITAK ULAKBIM, High Performance and Grid Computing Center (TRUBA resources). The routines and subroutines for the NEMD code are explained in this section. In this section, the steps of the NEMD code such as the creation of the structure, creating the slabs, MPI algorithm, calculating the temperature are explained.

2.2.1. Creating Atomistic Structures

The simulation domain consists of hundreds and thousands of atoms. These atoms are initially aligned according to their crystal structure. Depending on the element type the structure can be cubic, face-centred cubic (FCC) or honeycomb type. The FCC and honeycomb structures are created in C++ language as the first step of the NEMD code.

Carbon atoms that constitute graphene are aligned in the shape of a honeycomb where metal atoms are aligned in FCC shape. Structures can be seen in Figure 2.2.

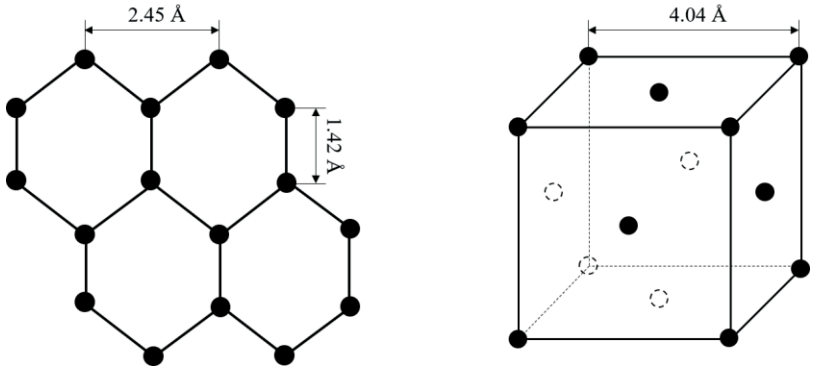

Figure 2.2 Representative scheme of the alignment of graphene and metal structure

In the code, each atom is identified with a coordinate and an atom number. These information's are written to a text file and read from that file before the NEMD code starts. The text file includes the total atom number of the system, type of the atom and cartesian coordinate information of all the atoms. An example of part of a structure file is shown in Figure 2.3.

```
1 1256
2
3 Al    0.000   0.000   0.000
4 Al    4.050   0.000   0.000
5 Al    8.099   0.000   0.000
6 Al    12.149  0.000   0.000
7 Al    16.198  0.000   0.000
8 Al    20.248  0.000   0.000
```

Figure 2.3 An example of part of a structure file for a simulation

As the energy flows from the heat source to the heat sink, a temperature gradient occurs on the simulation domain. Before starting the iterations, the sample region is separated into slabs. The temperature of each slab is calculated and summed at each time step. Mean values are written into a text file with a periodicity that is determined before.

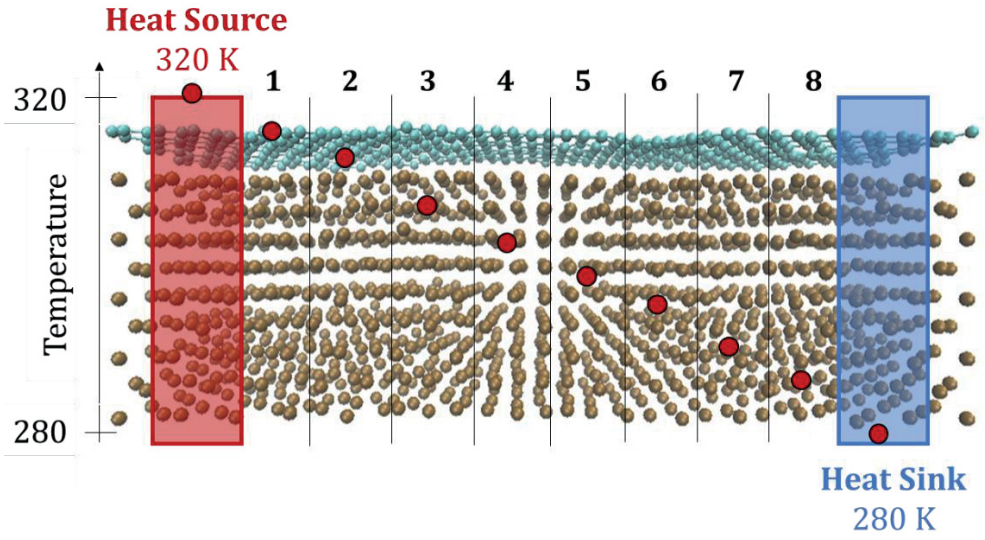

Figure 2.4 Representative schematic of a sample region divided into 8 equal slabs

Figure 2.4 shows an example of a sample region. This sample region is divided into 8 slabs meaning the temperature data is collected from 8 slabs separately at each time step. The calculation of temperature from kinetic energy will be explained in next subsections.

2.2.2. Interatomic Potentials

Although there are billions of atoms in a macroscopic system, properties of a macroscopic system can be obtained by modelling a microscopic system with fewer atoms and by using statistical thermodynamics. So that the motion of thousands of atoms can be simulated with great computational power. In an MD simulation, the trajectory of the atoms is obtained by using Newton's equation of motion. Equation 2.2 shows the formulation of Newton’s equation of motion.

$$m_i \frac{\partial^2 r_{ij}}{\partial t^2} = f_{ij} \tag{2.2}$$

In this equation i and j are the numbers of selected atoms, m is the mass, r is the position of the atom, t is the time and f is the force applied to the atom. Equation 2.2 shows that forces applied on each atom must be calculated to numerically solve $\frac{\partial^2 r_i}{\partial t^2}$ Partial Differential Equation (PDE). Atoms exert attractive and repulsive forces on each other depending on the distance between them. Equation 2.3 shows the calculation of interatomic forces. In this equation, U is the potential function which is an empirical mathematical function that represents the interatomic relation between atoms.

$$f_{ij} = -\frac{dU}{dr_{ij}} \tag{2.3}$$

The selection of appropriate potential function is necessary for modelling an atomic system and very first of these interactions is the Lennard-Jones potential. Lennard-Jones potential function and other potential functions are investigated below.

2.2.2.1. Lennard-Jones Potential

Lennard-Jones potentials is a pair potential. Pair potential means that the interaction between two atoms only depends on the distance between them. Other atoms in the system have no effect on the potential energy between those 2 atoms.

$$U_{tot} = \sum_i \sum_{j \neq i} U^{LJ}(r_{ij}) \tag{2.4}$$

A typical form of a pair potential is shown in Equation 2.4. The Lennard-Jones potential is a function that represents the interaction between two neutral atoms or molecules. Lennard-Jones potential function is shown in Equation 2.5.

$$U^{LJ} = 4\varepsilon\left[\left(\frac{\sigma}{r_{ij}}\right)^{12} - \left(\frac{\sigma}{r_{ij}}\right)^{6}\right] \tag{2.5}$$

Here, ε is the energy term that describes the strength of the interaction. σ is the distance between the particles that the potential is zero.

Figure 2.5 shows an example Lennard-Jones potential function changing with the distance between two atoms. One can clearly see that there is a strong repulsion as the particles come closer and small attraction as they move away. There is also a cut-off distance representing that there is no interaction between the particles after some distance. Cut-off distance r_c is generally selected as 2.5σ.

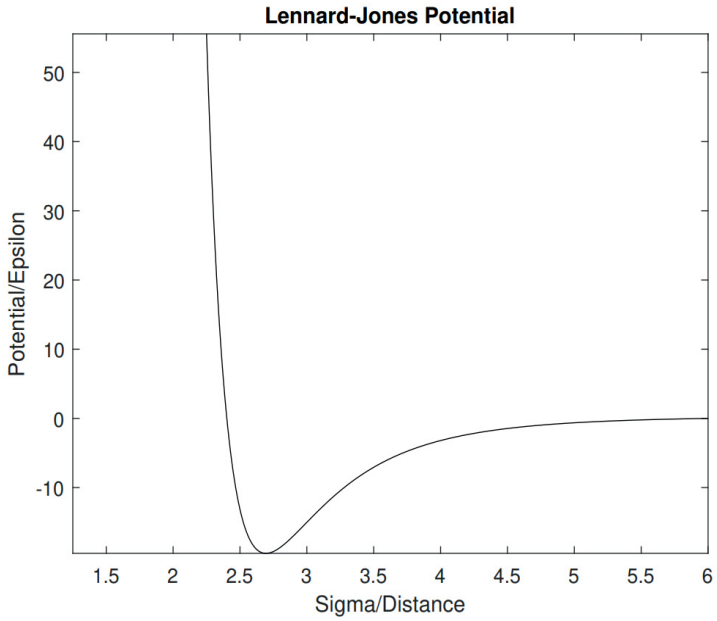

Figure 2.5 A typical graph of Lennard-Jones interatomic potential

So, the Lennard-Jones potential energy function becomes:

$$U^{LJ} = \begin{cases} 4\varepsilon\left[\left(\frac{\sigma}{r_{ij}}\right)^{12} - \left(\frac{\sigma}{r_{ij}}\right)^{6}\right], & r_{ij} < r_c \\ 0, & r_{ij} \geq r_c \end{cases} \tag{2.6}$$

The force acting on a particle is the derivation of the potential function with respect to r_{ij} and it is shown in Equation 2.7 for the Lennard-Jones potential (Filippova, Kunavin, and Pugachev 2015).

$$f_{ij} = \left(\frac{48\varepsilon}{\sigma^2}\right)\left[\left(\frac{\sigma}{r_{ij}}\right)^{14} - \frac{1}{2}\left(\frac{\sigma}{r_{ij}}\right)^{8}\right] r_{ij} \tag{2.7}$$

Once the force acting on particle *i* (f_{ij}) from particle *j* is calculated, the force acting on particle *j* from particle *i* (f_{ji}) can be calculated by using Newton's 3rd law of motion. So that, there is no need another calculation for f_{ji} which provides considerable computational time saving since there are thousands of particles in the simulation domain.

$$f_{ji} = -f_{ij} \tag{2.8}$$

Lennard-Jones potential is used for describing different interactions in the literature: Cu-C, C-C and Al-C (Kumar 2017; Rajabpour and Vaez Allaei 2012; Sidorenkov, Kolesnikov, and Saletsky 2016).

2.2.2.2. Sutton-Chen Potential

Sutton-Chen potential (Sutton and Chen 1990) is a many-body potential that is generally used for describing the interaction between metal particles. Many-body means that the interaction between atom *i* and atom *j* is not only a function of r_{ij} but also affected by locations of other atoms in the system. General form of the Sutton-Chen many-body potential is shown in Equation 2.9.

$$U_{tot} = \varepsilon \sum_i \left[\frac{1}{2}\sum_{j\neq i} V_{ij}^{pair}(r_{ij}) - c\sqrt{\rho_i}\right] \tag{2.9}$$

$$V_{ij}^{pair}(r_{ij}) = \left(\frac{\sigma}{r_{ij}}\right)^{n} \tag{2.10}$$

$$\rho_i = \sum_{j\neq i}\left(\frac{\sigma}{r_{ij}}\right)^{m} \tag{2.11}$$

U_{tot} is the total potential energy of the system and its unit is kJ/mole. Here, being different from a pair potential, ρ_i shows that Sutton-Chen potential does not only depend on the distance between two individual particles. It also depends on the position of the other particles in the system. In Equation 2.9, V_{ij}^{pair} is the pair potential part and it represents the repulsion force between particles, where ρ_i is the many-body potential part that approximately represents the force between particles caused by surrounding electrons (Liem and Chan 1995). ε, c and σ are parameters that are used for tuning the potential for different metals. Unit of ε is kJ/mole and unit of σ is Å. Derivative of the Sutton-Chen potential with respect to r is given in Equation 2.12.

$$f_{ij} = \varepsilon \left[n \left(\frac{\sigma}{r_{ij}} \right)^n - \frac{cm}{2} \left(\rho_i^{-1/2} - \rho_j^{-1/2} \right) \left(\frac{\sigma}{r_{ij}} \right)^m \right] \frac{r_{ij}}{r_{ij}^2} \tag{2.12}$$

In the literature, the Sutton-Chen potential is used for describing the interaction between metal atoms such as Al-Al (Deyirmenjian et al. 1995), Pt-C (Liem and Chan 1995). In 1998, Kimura et al. (Kimura et al. 1998) have modified the SC parameters for 9 FCC (Face Centered Cubic) metals and proposed the Q-SC (Quantum Sutton-Chen) parameters that are optimized for various properties. Q-SC parameters for some of these metals are given in Table 2.1.

Table 2.1 Q-SC parameters for some metals (Kimura et al. 1998)

Element	n	m	ε (eV)	c	σ (Å)
Ni	10	5	7.3767E-3	84.745	3.5157
Cu	10	5	5.7921E-3	84.843	3.6030
Pt	11	7	9.7894E-3	71.336	3.9163
Au	11	8	7.8052E-3	53.581	4.0651

2.2.2.3. Tersoff Potential

The Tersoff Potential is a many-body (3-body) potential that is used for modelling silicon and carbon structures. The difference of the Tersoff Potential from the SC and LJ

potentials is that it includes the angular contribution of the intermolecular force (Tersoff 1988). The general form of the Tersoff Potential is given in Equation 2.14.

$$U_{tot} = \frac{1}{2}\sum_{j \neq i} U^T \tag{2.13}$$

$$U_{ij}^T = f_{ij}^{\mathrm{C}}\left[a_{ij} f_{ij}^{\mathrm{R}} - b_{ij} f_{ij}^{\mathrm{A}}\right] \tag{2.14}$$

Here f_{ij}^C is the cut-off function, f_{ij}^R is the repulsive term and f_{ij}^A is the attractive term. Definitions of these terms are given below.

$$f^C(r_{ij}) = \begin{cases} 1 & r_{ij} < R_{ij} \\ \frac{1}{2} - \frac{1}{2}\cos\left[\frac{\pi(r_{ij}-R_{ij})}{S_{ij}-R_{ij}}\right] & R_{ij} < r_{ij} < S_{ij} \\ 0 & r_{ij} > S_{ij} \end{cases} \tag{2.15}$$

$$f_{ij}^{\mathrm{R}} = Ae^{(-\lambda_1 r_{ij})} \tag{2.16}$$

$$f_{ij}^{\mathrm{A}} = Be^{(-\lambda_2 r_{ij})} \tag{2.17}$$

Here, r_{ij} is the distance between atom *i* and atom *j*, *R* and *S* are minimum and the maximum cut-off distances, a_{ij} is the range limiting term and b_{ij} is the measure of the bond order.

$$b_{ij} = \left(1 + \beta^n \zeta_{ij}^n\right)^{-1/2n} \tag{2.18}$$

$$\zeta_{ij} = \sum_{k \neq i,j} f^{\mathrm{c}}(r_{ik}) g\left(\theta_{ijk}\right) \tag{2.19}$$

$$g\left(\theta_{ijk}\right) = 1 + \left(\frac{c}{d}\right)^2 - \frac{c^2}{d^2 + \left[h - \cos\theta_{ijk}\right]^2} \tag{2.20}$$

Here, θ_{ijk} is the angle between *ij* and *ik* bonds. The values for other parameters are given in Table 2.2 (Rajasekaran, Kumar, and Parashar 2016a).

Table 2.2 Tersoff Potential parameters for C-C bonding interactions

A [eV]	B [eV]	λ_1 [Å]	λ_2 [Å]	n	c
1393.6	346.74	3.4879	2.2119	0.72751	38049
d	h	β	R_{ij} [Å]	S_{ij} [Å]	a_{ij} [Å]
4.3484	-0.57058	1.5724×10^{-7}	1.8	2.1	1

2.2.3. Thermostat

NEMD simulation starts with setting the system temperature to the desired value. This is done by a thermostat that is implemented in the Verlet Algorithm which is mentioned in Section 2.2.5. In this thesis, Nose-Hoover thermostat is used.

The idea of Nose-Hoover thermostat (Nosé 1984) is introducing a dynamical friction parameter, ζ, that changes according to the desired level of temperature and the current temperature of the system. Calculations of friction acceleration and the friction velocity are given below.

$$\ddot{\zeta} = \left[\left(\frac{T}{T_{set}}\right) - 1\right] * \tau \tag{2.21}$$

$$\dot{\zeta} = \dot{\zeta} + \ddot{\zeta} * \Delta t/2 \tag{2.22}$$

Equation 2.21 and Equation 2.22 shows the friction acceleration $(\ddot{\zeta})$ and friction velocity $(\dot{\zeta})$ where T is the current temperature, T_{set} is the desired temperature and τ is the damping constant. These values are calculated at each time step and used in the Verlet algorithm. Rearranged version of the Verlet Algorithm for Nose-Hoover thermostat is given below.

$$v(t + \Delta t/2) = v(t) * e^{-\dot{\zeta} * \Delta t/2} + a(t)\Delta t/2 \tag{2.23}$$

$$r(t + \Delta t) = r(t) + v(t + \Delta t/2)\Delta t \tag{2.24}$$

$$a(t + \Delta t) = F\big(r(t + \Delta t)\big)/m \tag{2.25}$$

$$v(t+\Delta t) = (v(t+\Delta t/2) + a(t+\Delta t)\Delta t/2) * e^{-\dot{\zeta}*\Delta t/2} \quad (2.26)$$

When the simulation starts, Nose-Hoover thermostat continuously tries to adjust the temperature to T_{set}. Figure 2.6 shows the effect of τ on the overall temperature of the system. In Figure 2.6, deviation in the temperature is much more when τ = 50. When τ is selected as 10, system shows a better conversion to the T_{set} value.

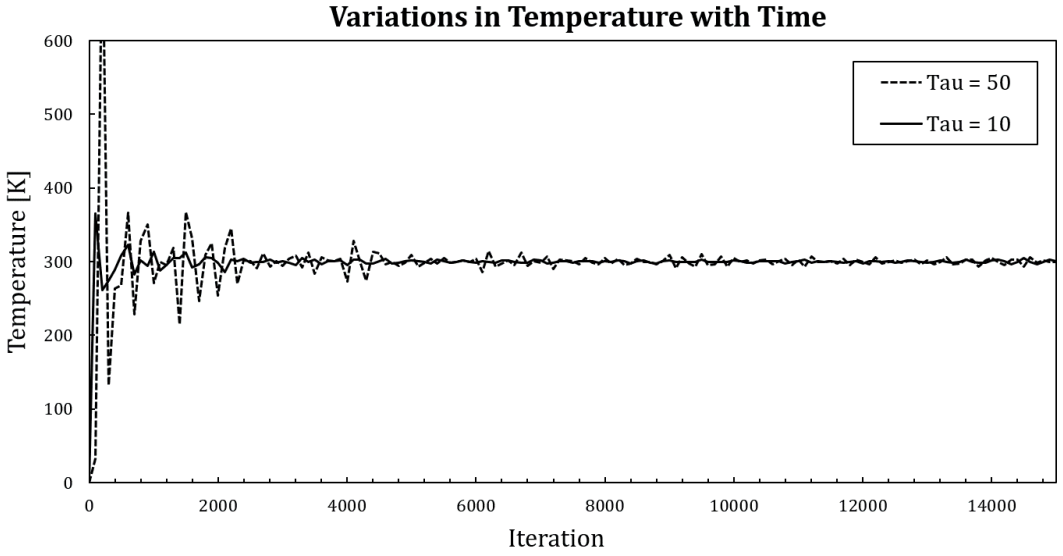

Figure 2.6 Temperature change along simulation time for two different τ values

2.2.4. Massage Passing Interface

Massage Passing Interface (MPI) is a message passing protocol that is used to run parallel programs (Gropp et al. 1999). In this project, the MPI algorithm is implemented to the NEMD code for saving time. Calculating the interactions between thousands of atoms is a huge work and MPI algorithm enables sharing this work with several processes. NEMD code creates the desired number of processes by using MPI and distributes the atoms in the system to each process. Each process runs the code for the atoms it is responsible for and shares the necessary information with other processes. This is done by several commands of MPI protocol. Some of the communication commands used in this NEMD code are MPI_Allreduce, MPI_Allgatherv, and MPI_Barrier. MPI_Allreduce is a command that collects the relevant data from all processes and does the operation (summing, extracting, dividing etc.) meanwhile. This command is used for summing the

forces acting on each atom from each process. MPI_Allgatherv is used for sending an array of information (positions, velocities or accelerations of atoms) to each process. MPI_Barrier is used as a barrier for processes that complete the job. Once a process completes the job, it waits for other processes to complete to move on the next task.

2.2.5. Time Integration

In an MD simulation, the equations of motion must be integrated to obtain meaningful results about the system. Taylor series is one way of doing the integration process. The general form of the Taylor series expansion is shown in Equation 2.27.

$$f(x+\Delta x) = f(x) + \frac{\Delta x}{1!}f'(x) + \frac{(\Delta x)^2}{2!}f''(x) + \cdots + \frac{(\Delta x)^n}{n!}f^n(x) + O(\Delta x^{n+1}) \tag{2.27}$$

The Verlet integration method (Verlet 1967) is one of the integration methods that is widely used for predicting the time trajectory of the atoms in an MD simulation. Verlet integration uses the Taylor Series Expansion. If Equation 2.27 is solved for both position and the velocity, we can obtain Equation 2.28 and Equation 2.29.

$$v(t+\Delta t) = v(t) + a(t)\Delta t + O((\Delta t)^2) \tag{2.28}$$

$$r(t+\Delta t) = r(t) + v(t)\Delta t + \frac{1}{2}a(t)(\Delta t)^2 + O((\Delta t)^3) \tag{2.29}$$

Leapfrog version of Verlet integration method is generally preferred due to its advantages of higher stability and lower memory requirements. Leapfrog Verlet equations are shown in the equations below.

$$v(t+\Delta t/2) = v(t) + a(t)\Delta t/2 \tag{2.30}$$

$$r(t+\Delta t) = r(t) + v(t+\Delta t/2)\Delta t \tag{2.31}$$

$$a(t + \Delta t) = F\big(r(t + \Delta t)\big)/m \tag{2.32}$$

$$v(t + \Delta t) = v(t + \Delta t/2) + a(t + \Delta t)\Delta t/2 \tag{2.33}$$

Trajectory of the atoms in a system can be calculated by using appropriate interatomic potentials and integrating Newton's equation of motion by using integration methods. Obtained data can be used for investigating desired properties of the materials.

2.2.6. Calculation of Temperature

Thermodynamic properties of materials can be calculated from the data collected from atoms movements. These thermodynamic properties can be entropy, internal energy or temperature. Velocities of atoms are calculated with Verlet integration and the total kinetic energy of the system of each slab is calculated with kinetic energy formula which is shown in Equation 2.34.

$$E_{kin} = \sum_{i=1}^{N} \frac{1}{2} m_i v_i^2 \tag{2.34}$$

Temperature is calculated by using Equipartition Theorem shown in Equation 2.35, where *N* is number of atoms in the system, k_b is Boltzmann Coefficient, m_i is the mass of atom *i* and v_i is the velocity of atom *i*. Averaging the temperature values for each slab leads to a temperature profile across the model.

$$\frac{3}{2} N k_b T = \sum_{i=1}^{N} \frac{1}{2} m_i v_i^2 \tag{2.35}$$

Example of a temperature gradient is shown in Figure 2.7 is used to calculate the thermal conductivity of the material.

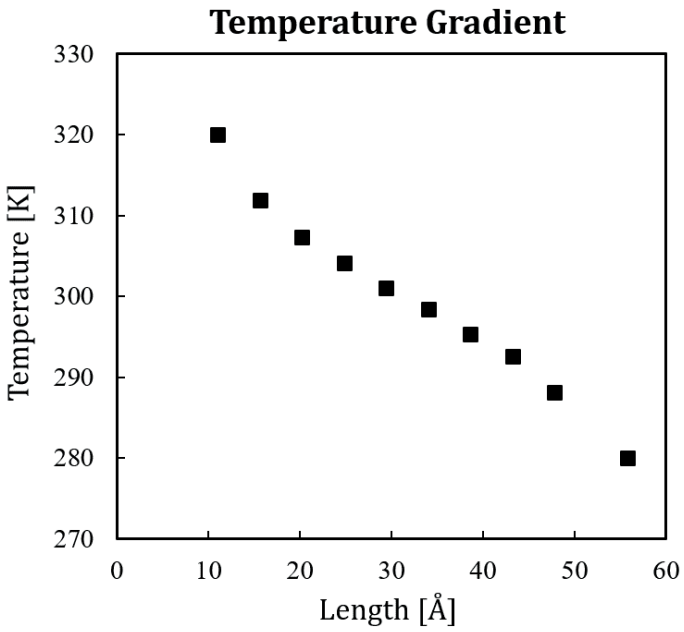

Figure 2.7 An example of the temperature distribution across a model

In the final stage of the NEMD code, all the data collected from the simulation is used to calculate the κ_{ph}. Fourier's law of conduction is used for this calculation.

$$k_{ph} = \frac{\Delta E_{avg}}{A \Delta t \frac{dT}{dx}} \tag{2.36}$$

Here, *A* is the cross-sectional area of the material, *t* is the time interval of the used data, $\frac{dT}{dx}$ is the temperature gradient and ΔE_{avg} is the heat energy. The heat flux is calculated by computing the added and extracted energy during the simulation. Energy change of heat source and heat sink are calculated by Equation 2.37 and Equation 2.38 respectively.

$$\Delta E_{src} = \sum_{heatflux} \frac{1}{2} m_i \left(\sum_{N_{src}} v_{\text{i,new}}^2 - \sum_{N_{\text{src}}} v_{\text{i,old}}^2 \right) \tag{2.37}$$

$$\Delta E_{snk} = \sum_{heatflux} \frac{1}{2} m_i \left(\sum_{N_{snk}} v_{\text{i,new}}^2 - \sum_{N_{\text{snk}}} v_{\text{i,old}}^2 \right) \tag{2.38}$$

Since the energy must be conserved, energy entering the system (ΔE_{src}) must be very close to energy leaving the system (ΔE_{snk}). The average of these values is $\left(\Delta E_{avg}\right)$ which is shown in Equation 2.39.

$$\Delta E_{avg} = \frac{\Delta E_{src} + \Delta E_{snk}}{2} \tag{2.39}$$

CHAPTER 3

MATERIALS & METHODS

In this chapter, the details of the molecular dynamics simulation and experimental setup will be given. For the numerical part: model dimensions, simulation methodology and code layout; for the experimental part: the experimental setup, the technical drawings and the equipments will be explained in detail.

3.1. Numerical Modelling

In this thesis, C++ language is used for all the programming. In this section, the details of the NEMD program and the program layout is reported. Several parts from the NEMD code is shared in the Appendices section.

3.1.1. Atomistic Structures

In this thesis, 3 different types of models and their variations are investigated numerically. These models are graphene, aluminium and graphene-coated aluminium. The preparation of the models is explained in Section 2.2.1. Molecular structures of the models are given in Figure 3.1.

In Figure 3.1, (a) is the pure aluminium model, (b) is SLG coated aluminium (SLG) with zig-zag edge orientation, (c) is five-layer graphene coated aluminium and (d) is single-layer graphene. Zig-zag edge orientation is used for all the simulations. Also, Figure 3.3 shows the atomistic structures of defected models: a) horizontally aligned rectangular graphene defect, b) randomly distributed point defect on graphene, c) vertically aligned rectangular graphene defect, d) crosswise aligned rectangular graphene defect, e) horizontally aligned rectangular defect on graphene-coated aluminium, f) randomly distributed point defect on graphene-coated aluminium, g) vertically aligned

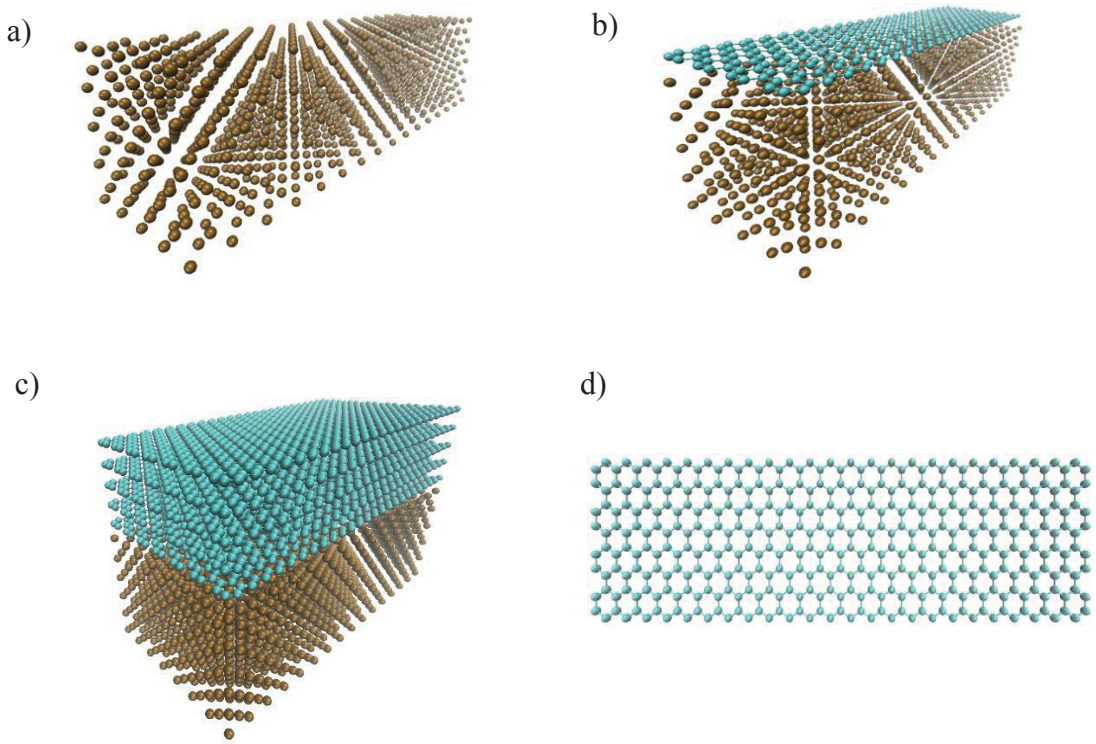

Figure 3.1 Molecular structures of the models used for simulations

rectangular defect on graphene-coated aluminium, h) crosswise aligned rectangular defect on graphene-coated aluminium.

In Figure 3.2, important parts of the model and the significant dimensions are given. The model consists of 5 sections: 2 error slabs, a heat source, a heat sink and a main slab. Error slabs are placed at both edges of the models in order to prevent the edge effects. The heat source and the heat sink are created for adding and extracting energy for creating the temperature gradient across the structure.

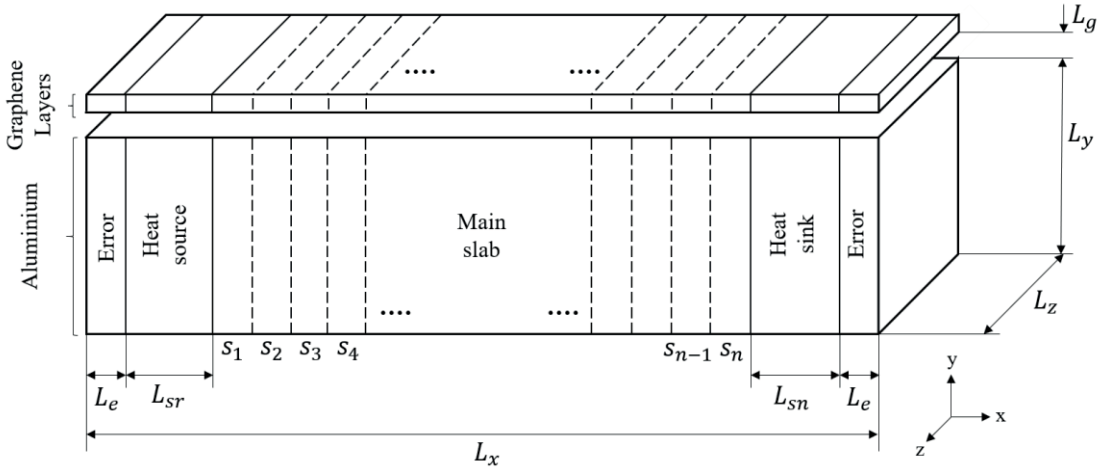

Figure 3.2 Representative schematic of the graphene coated aluminium model

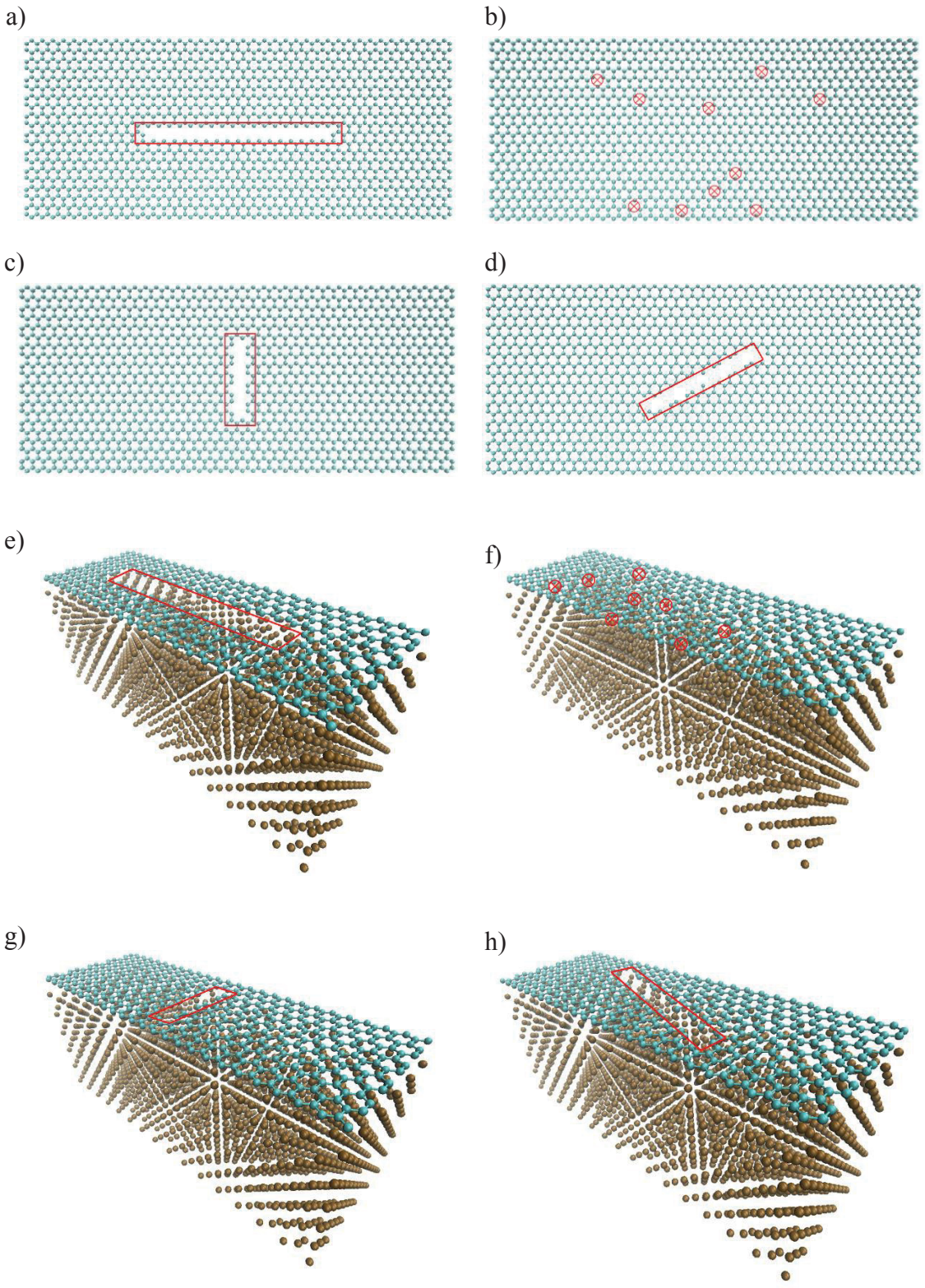

Figure 3.3 Atomistic structures of defected models

In Figure 3.2, main slab is the part between heat source and heat sink which is the part that temperature data is collected during the simulation. Here, n is the number of equally divided slabs which are created in the main slab section. L_e is the length of the

error slabs, L_{sr} and L_{sn} are lengths of the heat source and heat sink slabs. L_x, L_y and L_z are the length, width and height of the aluminium model. L_g is the distance between aluminium block and the first graphene layer. Finally, the distance between different graphene layers is L_{gr}. Dimensions are listed in Table 3.1.

Table 3.1 Common structure dimensions for all simulations

L_g [Å]	L_{gr} [Å]	L_{sr} [Å]	L_{sn} [Å]	L_e [Å]	n
3 (Kumar 2017)	3.4 (Wei et al. 2011a)	8	8	3	6

The interactions between carbon atoms which are in the same graphene layer are calculated with Tersoff Potential shown in Equation 2.14. Tersoff Potential parameters for C-C bonding (Rajasekaran, Kumar, and Parashar 2016b) are listed in Table 2.2.

Finally, Harmonic potential shown in Equation is used for simulating single and multilayer graphene to prevent graphene layers to move undesirably during the simulation. Harmonic potential is applied to the atoms that are at the corners of the graphene sheets.

$$U^{\mathrm{H}} = \frac{1}{2} k_h (r_{ij} - r_0)^2 \tag{3.1}$$

Harmonic potential constants k_h and r_0 for carbon atoms are selected as 3925 $\frac{kJ}{mol*\text{Å}^2}$ and 1.42 Å respectively. All the potentials used in simulations are shown in Figure 3.4.

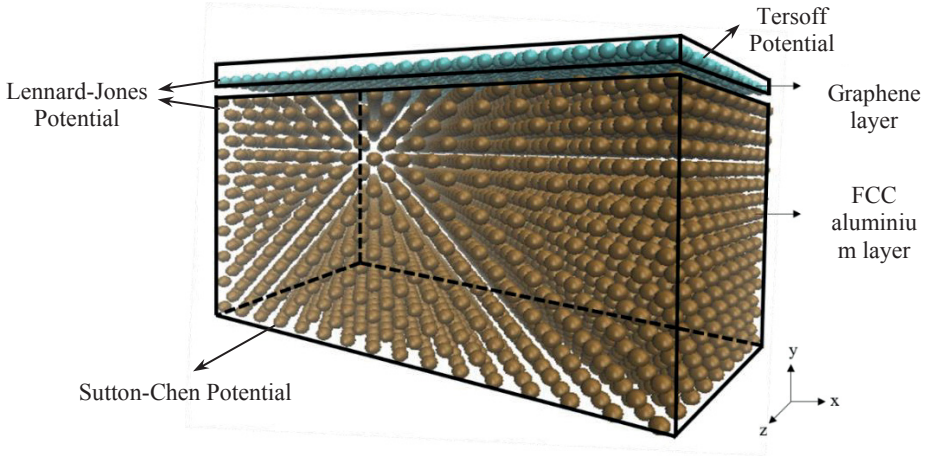

Figure 3.4 Interatomic potentials for simulations

3.1.2. Code Structure

Simulations are conducted in two phases. In the first phase, all the slabs are heated up to 300 K. In the second phase, heat source slab is heated to 320 and heat sink slab is cooled down to 280 K. The Nose-Hoover thermostat mentioned in Section 2.2.3 is used for heating and cooling the system. The relaxation time (τ) is selected as 10 *fs*. The numerical integrations are calculated by using The Velocity Verlet integration shown in Section 2.2.5. The timestep is selected as 0.5 *fs* for all the simulations.

Algorithm 1 NEMD Code

initialize the structure;
create desired number of slabs;
initialize MPI algorithm;
while $time < time_{init}$ **do**
  calculate forces;
  verlet integration with thermostat; $\rightarrow T_{set} = 300K$
  calculate temperature;
  print data;
  $time$++;
end while
while $time < time_{end}$ **do**
  calculate forces;
  verlet integration with thermostat; $\rightarrow T_{src} = 320K, T_{snk} = 280K$
  calculate temperature;
  print data;
  $time$++
end while
finalize MPI algorithm;

Figure 3.5 Structure of the NEMD code

Figure 3.5 shows the layout of the main steps of the NEMD code. Before the simulation starts, the structure is created; slab boundaries are determined according to the number of slabs and MPI is initialized. In the beginning, the simulations are run 0.125 ns to achieve a system temperature at 300K. For this, firstly, the forces exerted to each atom in the system are calculated with appropriate potential. Then, new locations of each atom are calculated by Verlet integration.

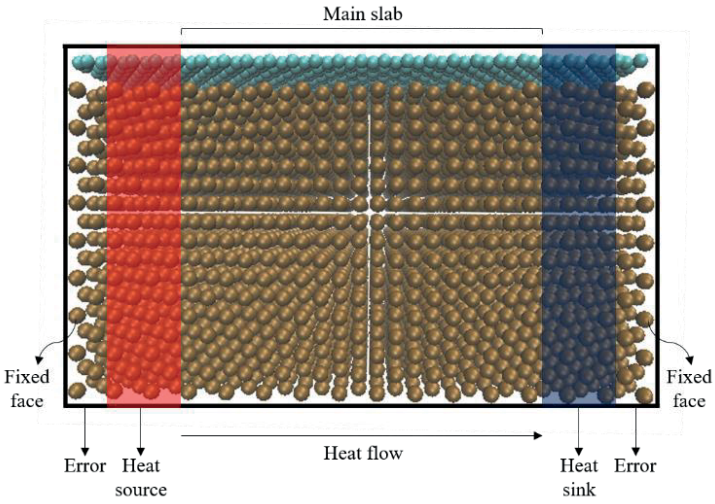

Figure 3.6 Detailed side view of atomistic structure of graphene coated aluminium model

Finally, the temperature is calculated and recorded. As the system reaches to 300K, heat source at 320 K and heat sink at 280 K are applied to the system for 15000 ns. Finally, as the system reaches to steady-state, the collected data is used to calculate the thermal conductivity.

3.2. Experimental Setup

In this thesis, the thermal performance of two materials are investigated experimentally: First material is A360-commercial aluminium. The second material is graphene reinforced A360 Al alloy. The experimental setup is designed to observe the thermal performance of graphene reinforced sample and compare with A360 Al. Thus, a forced convection heat transfer setup is designed and produced. Figure 3.7 shows the representation of the experimental setup.

In Figure 3.7, a water tank is filled with water and a resistance heater is placed inside the tank. Resistance heater is controlled with a PID temperature controller device. A diaphragm pump is used to pump the heated water from the water tank to the heat exchanger. The heat exchanger is a finned tube heat exchanger and it is placed right in front of the fan to heat the incoming air. Air is transferred through a pipe to the sample holder where the sample is located for testing. A Peltier heater is used to heat the sample. Both the peltier heater and the fan are powered by a power supply. Air is then transferred to ambient. In the setup, Kontel HRC 1-M model PID temperature controller is used to

control the resistance heater located in the water tank. Water is heated to the desired level of temperature to heat the air for different test condition purposes. 12 V, 5.3 A computer fan is used to transport the air through the pipe. Fan is controlled with the power supply and air speed at the outlet of the channel is measured with Testo 435 hotwire anemometer. Measurements are taken with mean values for 10 second data. Air speed and Reynolds number change according to fan voltage is shown in Appendix C. It is observed that the temperature difference for inlet and outlet is only achieved with the low air speeds. Hence, the experiments are conducted in the range of 4.4-7 V and 0.5-1.04 m/s air speed.

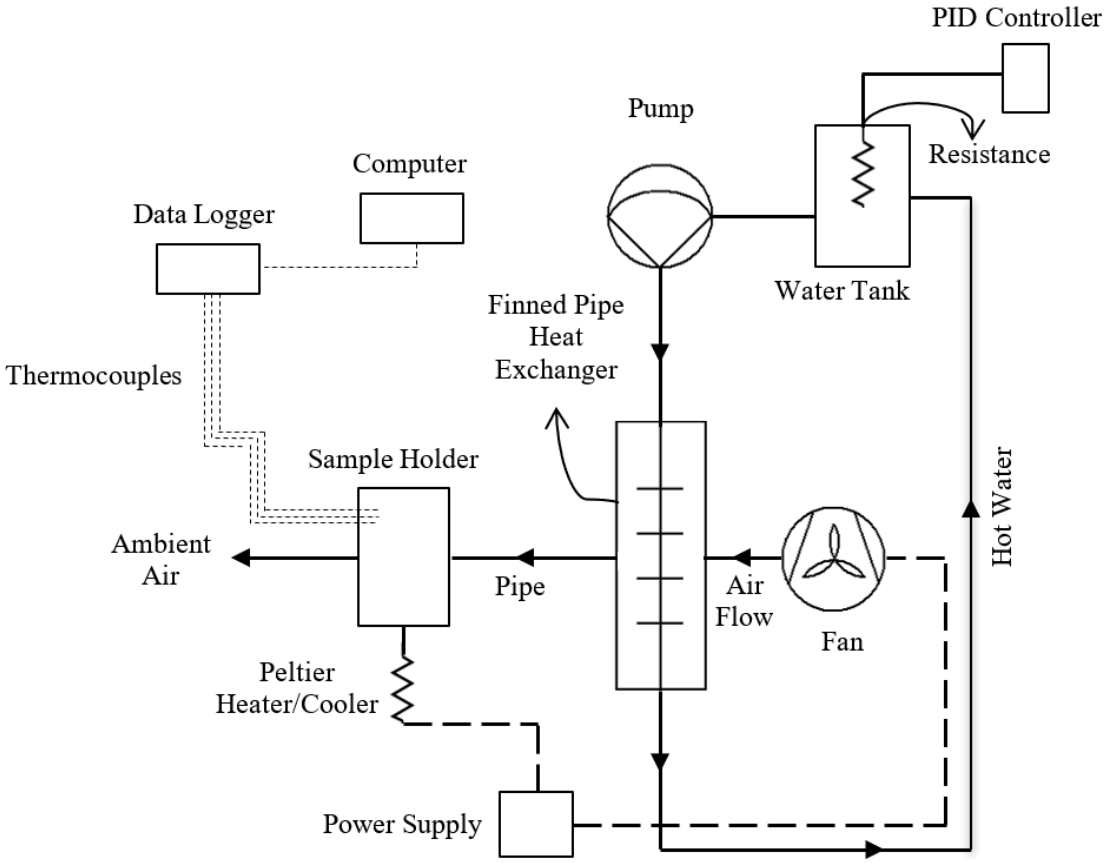

Figure 3.7 Schematic representation of the experimental setup

Airspeed is controlled by changing the voltage from power supply. TEC1-12705 Peltier is placed under the sample and the peltier heater is also connected to the power supply. 6 K-Type thermocouples are used for temperature measurement. LabJack U6 model data logger is used to read analogue output from thermocouples. Plastic plumbing pipes and jointing apparatuses are used as air channel.

3.2.1. Sample Production

In this work, graphene nanoplatelet (GNP) reinforced aluminium metal matrix composite is produced with a combination of stir casting and ultrasonic mixing. The samples are in cylindrical form with a diameter of 13 mm and height of 22 mm. Pictures of samples are shown in order in Figure 3.8.

Figure 3.8 Al360 and GNR reinforced Al samples

Sample production starts with melting A360 alloy in graphite crucible by a resistance furnace which is followed by adding GNP and Al powder in form of tablets. Next, ultrasonic mixing is applied to achieve homogenous GNP distribution in AMMC (Martin, Kandemir, and Antonov 2020). Scanning Electron Microscope (SEM) image of GNP reinforced A360 alloy is given in Figure 3.9.

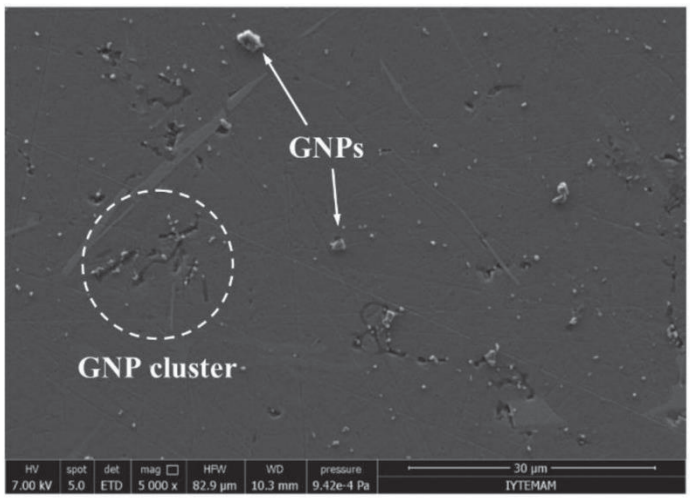

Figure 3.9 SEM image of Al360/0.5wt.% GNP composite (Martin, Kandemir, and Antonov 2020)

3.2.2. Sample Holder Design

The sample holder is designed and produced to locate the sample properly and to place the thermocouples. The sample holder is manufactured by a 3D printer. Sample holder consists of two parts. Bottom part is for placing the sample, thermocouples and peltier heater where the upper part is for airflow. Figures show the 3D models of the two parts of the sample holder drawn in SolidWorks.

In Figure 3.10, square-shaped space is created for locating the peltier heater. The hole under the peltier cell is created for airing the hot/cold side of the peltier. Thermocouple holes are used for passing the thermocouples through and attaching to the surface of the sample.

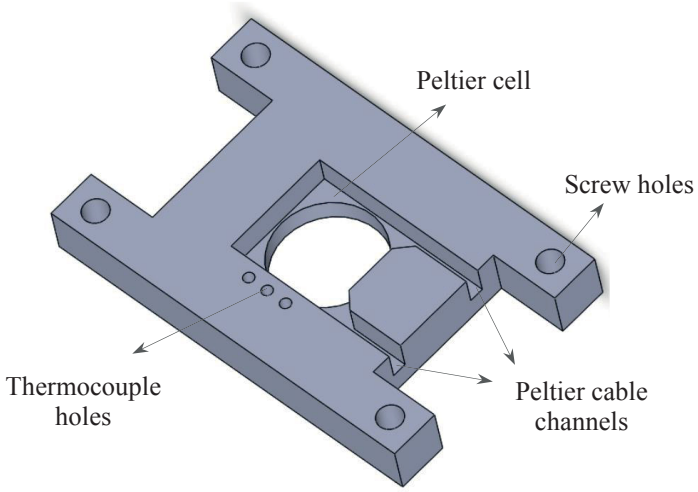

Figure 3.10 3D model of bottom part of the sample holder

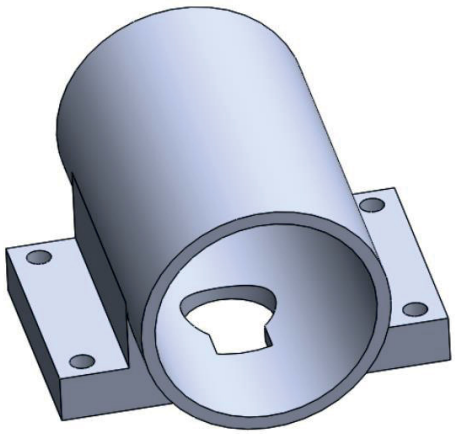

Figure 3.11 3D model of the upper part of the sample holder

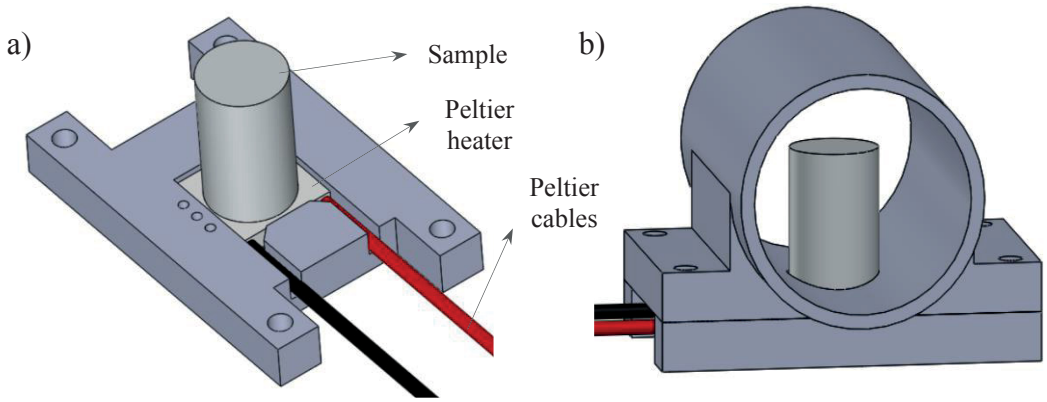

Figure 3.12 3D models of the sample holder: a) bottom part b) final assembly

Figure 3.11 shows the upper part and the final assembly of the sample holder. Figure 3.12 shows the final assembly with the sample and the heater placed. In Figure 3.12 (a), the sample is located on the peltier heater and peltier heater is placed right onto the peltier cell mentioned in Figure 3.10. Since the sample has a rough surface due to the production, HY510 model thermal paste (1.93 W/mK) is used between the sample and the heater to achieve better heat flow. All the possible air outlets are sealed with a liquid gasket. The pipe diameter kept as small as possible to observe the heat transfer from the sample to air better. Technical drawings of the sample holder are given in Appendix A.1 and A.2.

3.2.3. Methodology

Thermocouples are placed in the sample holder to collect the data from the sample and to measure inlet and outlet temperature difference. Figure 3.13 shows the schematic of the sample and thermocouple placement in the sample holder. As the first step in the experiment, the peltier heater is powered for heating/cooling the samples and waited until the sample reaches to steady-state condition. Figure 3.14 shows the thermocouple values as the system reaches to steady-state. After sample temperatures T3, T4 and T5 values converge to a significant value, the water heater is started to heat the water to the desired temperature for managing the air inlet temperature T1. Water is pumped into a finned tube heat exchanger which is placed in front of the fan. The inlet temperature is set to 20°C and 30°C for heating and cooling experiments respectively. As the inlet temperature

reaches to the desired value, the fan is started at the lowest speed and waited for the system reaches to steady-state temperature.

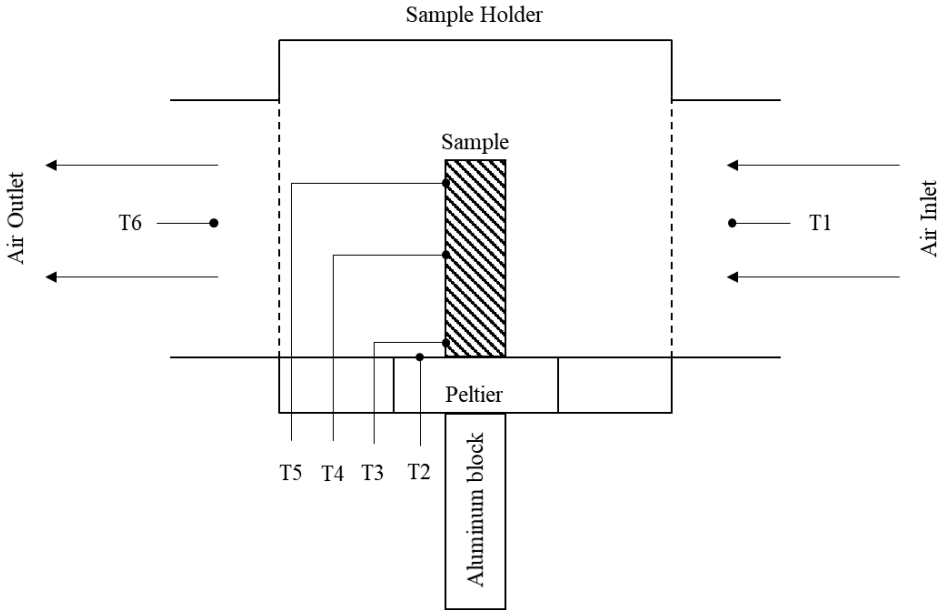

Figure 3.13 Schematic of thermocouple placements in the sample holder

At this point, the temperature data is collected for 30 seconds and mean values are used to calculate absolute temperature difference, |T6-T1|. Temperature difference is measured for different airspeeds by increasing the fan voltage 0.2 V at each step. The aluminium block is used for heat dissipation from the hot/cold side of the heater to not harm the peltier.

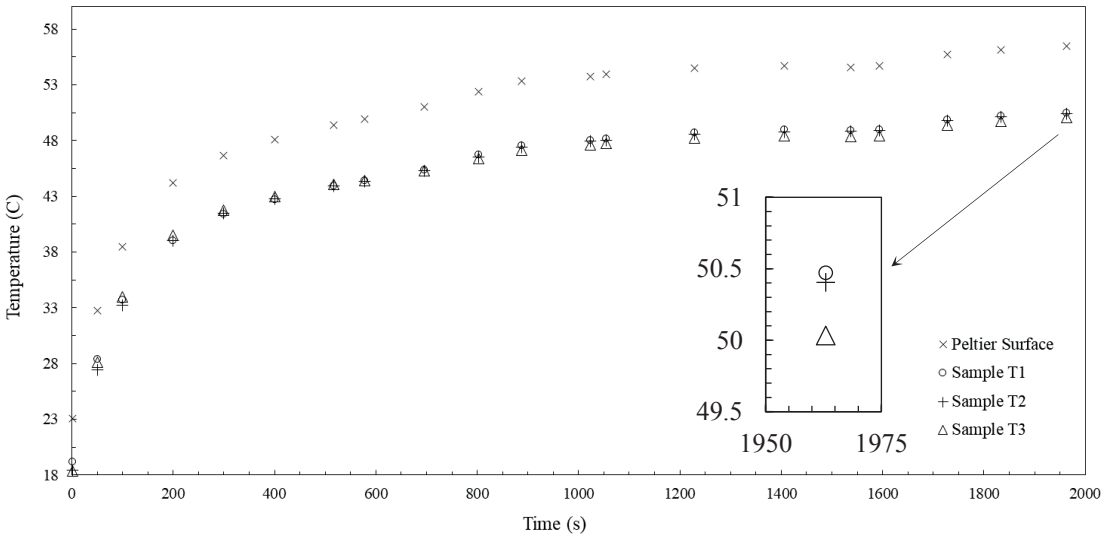

Figure 3.14 Steady-state temperature distribution for the Gr-Al sample

Proper temperature distribution could not be achieved on the sample. This is due to very short sample length (2.2 cm). 55 ℃ of base temperature achieved with the peltier heater. Pictures of the experimental setup is given in Figure 3.15 and Figure 3.16.

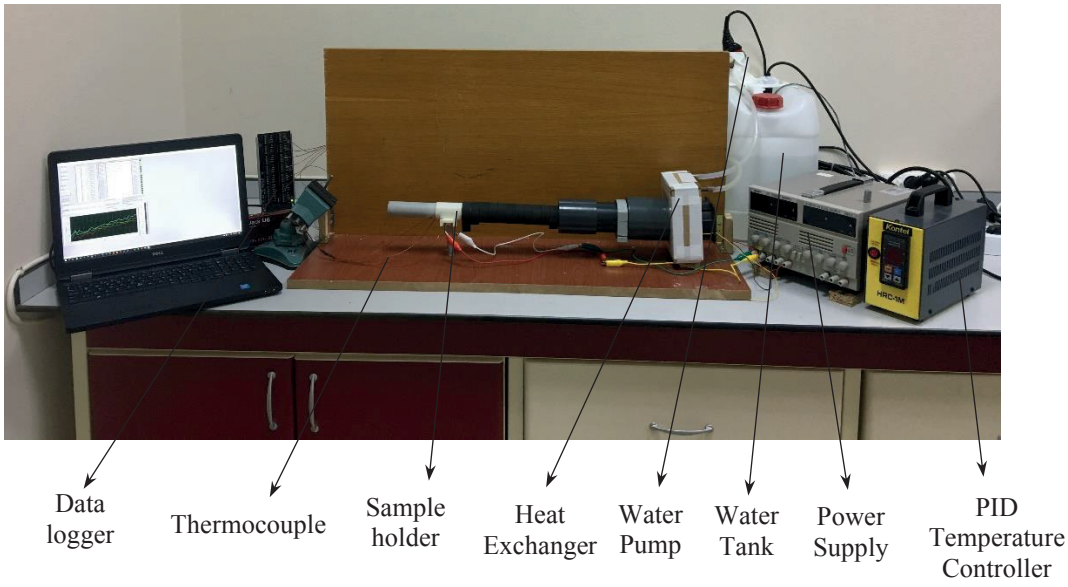

Figure 3.15 Picture of the experimental setup

a) b)

Figure 3.16 Zoom-in pictures of the experimental setup a) control units, b) sample holder

CHAPTER 4

RESULTS

In this chapter findings of numerical simulations and experiments is shared and discussed.

4.1. Numerical Results

In this section, the results of NEMD simulations will be presented. First, simulations are made for validating the NEMD code with similar studies from the literature. Hence, pure aluminium and graphene models are tested with length dependency and compared with the literature.

4.1.1. Pure Aluminium

Starting from the aluminium, the length effect on κ_{ph} is investigated. For this test, the height and the width of the aluminium block are selected as 20 Å × 20 Å. Figure 4.1 shows the change of κ_{ph} of aluminium with length.

Figure 4.1 shows that κ_{ph} of aluminium increases from 2.9 $Wm^{-1}K^{-1}$ to 3.4 $Wm^{-1}K^{-1}$. There is no experimental study investigating the phonon thermal conductivity of metals. However, there are several MD studies available for comparing the results. For example, one of these studies showed that κ_{ph} of pure aluminium changes between 2 $Wm^{-1}K^{-1}$ and 5 $Wm^{-1}K^{-1}$ as the length increases from 25 Å to 100 Å (Chantrenne, Raynaud, and Barrat 2003b). In another study, it is reported that κ_{ph} of aluminium changes between 1-7 $Wm^{-1}K^{-1}$ as the length increases 0 Å to 200 Å (Ya Zhou, Anglin, and Strachan 2007). In metals, heat transfer is dominated by electrons rather than phonons. This is due to mean free path of electron interactions are greater than the phonon-phonon interactions. So, phonon thermal conductivity constitutes a very small part of the overall thermal conductivity.

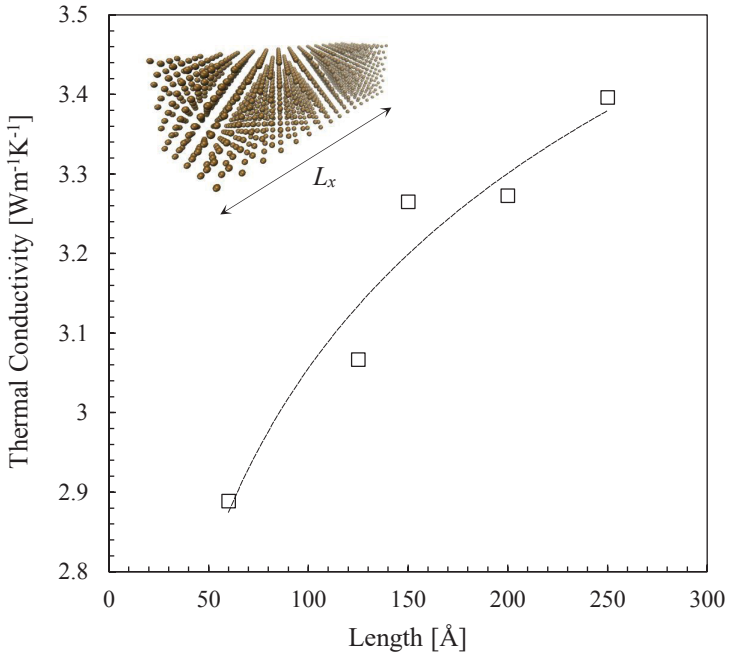

Figure 4.1 Length effect of thermal conductivity of pure aluminium

In addition to the length effect, the width and the height effects are also investigated. The results are shown in Figure 4.2.

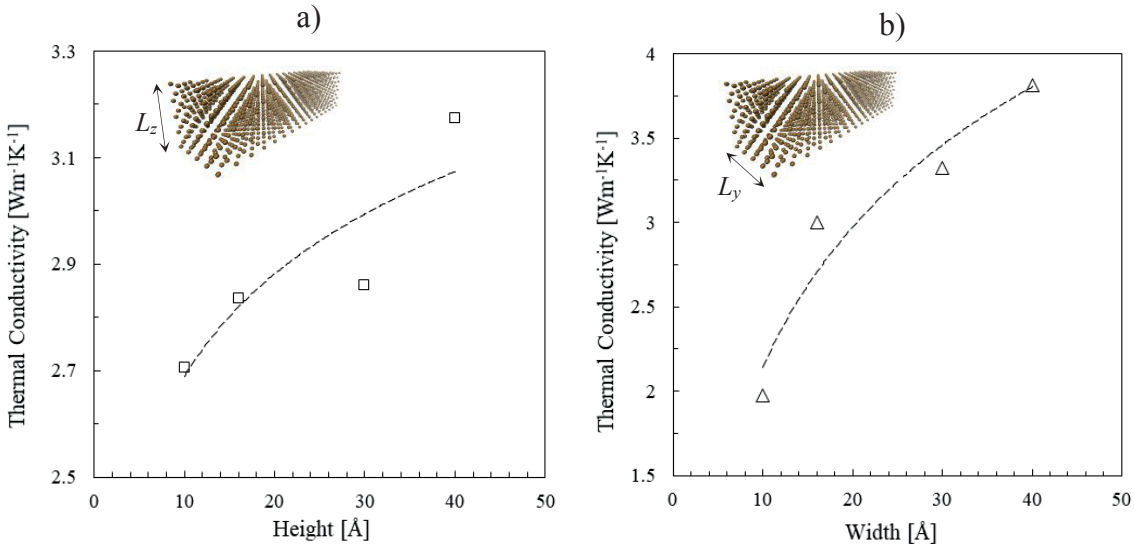

Figure 4.2 Height (a) and width (b) effect on thermal conductivity of pure aluminium

In Figure 4.2, κ_{ph} of aluminium increases up to 3.2 $Wm^{-1}K^{-1}$ and 3.7 $Wm^{-1}K^{-1}$ as the height and width increases from 10 Å to 40 Å respectively.

4.1.2. Graphene

For graphene, simulations are made for temperature, length dependence, layer number, defect number, defect size and defect shape. First simulations are made for comparing the results with another study from the literature (Wei et al. 2011b). To do so, graphene lengths and most of the simulation properties are selected same with the mentioned study. The thickness of the graphene layer is assumed to be 3.4 Å for the final calculation of κ_{ph}. Figure 4.3 shows the comparison of the results from this work and reference study.

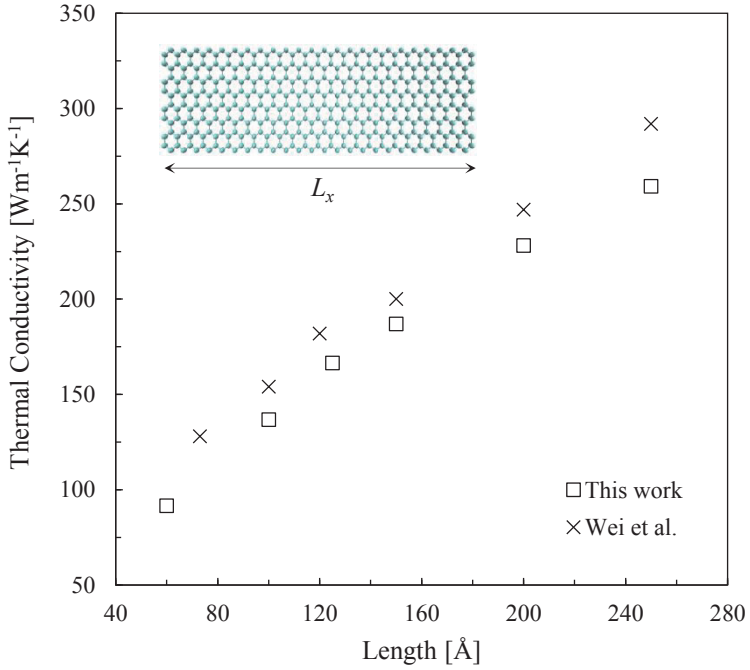

Figure 4.3 The comparison of the thermal conductivity results with reference work for SLG

The maximum thermal conductivity difference with the reference work is observed at 250 Å model length and it is 11.5%. By power law fitting the data points in Figure 4.3, it is calculated that the κ_{ph} follows the curve of $\kappa_{ph} \sim {L_x}^{0.5}$. For the reference work this relation is calculated as $\kappa_{ph} \sim {L_x}^{0.66}$. The differences partially arise from the unchanged parameters due to the lack of information in the reference paper.

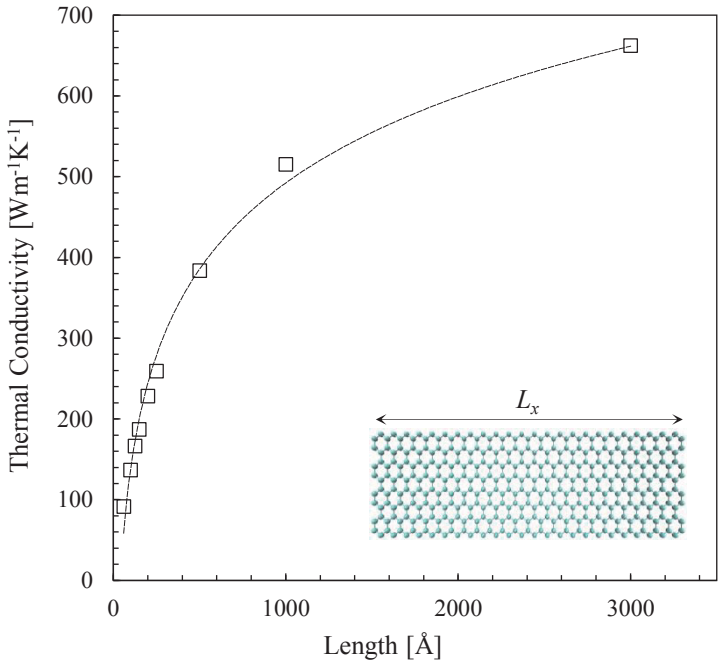

Figure 4.4 Length effect on thermal conductivity of suspended graphene

Figure 4.4 shows the κ_{ph} change of single layer graphene with a length varying from 60 Å to 3000 Å. κ_{ph} of graphene increases from 91 $Wm^{-1}K^{-1}$ up to 662 $Wm^{-1}K^{-1}$. According to the results, κ_{ph} of SLG is ~200 times greater than pure aluminium. This is because, in graphene, heat transfer is dominated by phonons on the contrary of metals. Temperature distribution along the graphene layer is shown in Figure 4.5.

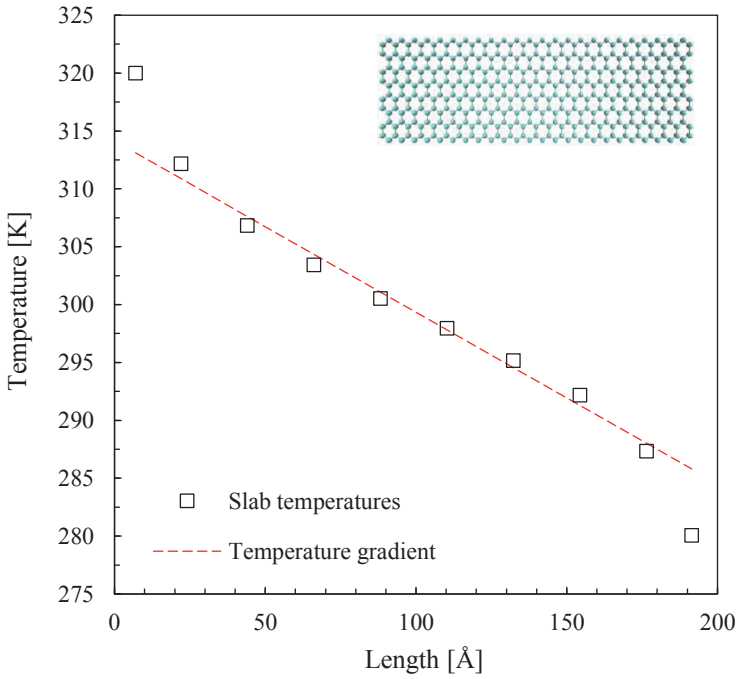

Figure 4.5 Temperature gradient across 200 Å suspended graphene layer

Temperature jumps at the edges of graphene layer can also be seen from Figure 4.5. This phenomenon arises due to the phonon mean free path (PMFP) of graphene. Mean free path (MFP) is the maximum distance taken by a moving particle (electron, atom, photon or atom) between two collisions. So PMFP is the distance phonons take before a collision. Phonon mean free path of graphene is reported to be ~775 nm (Ghosh et al. 2008). Since the length of the graphene layer model used for this work is too short (6 to 300 nm) comparing to PMFP of graphene, heat source and heat sink limits the PMFP. This results in the phonons travel ballistically and create the temperature jumps at the edges of the graphene layer.

Finally, temperature effect on SLG is investigated. For this, system thermostats are arranged varying between 100 K and 800K. Figure 4.6 shows the change of κ_{ph} according to system temperature.

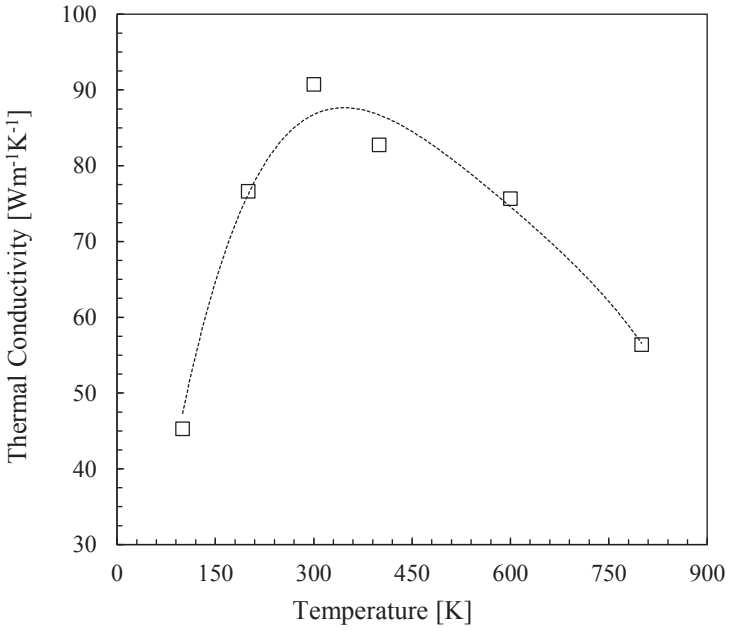

Figure 4.6 Temperature effect on thermal conductivity of SLG

Figure 4.6 shows that κ_{ph} of SLG increases from 100K to 300 K and reaches its maximum point. κ_{ph} decreases monotonically after 300 K and reaches 56 $Wm^{-1}K^{-1}$ with a 37% reduction. It is shown that κ_{ph} of graphene highly dependent to system temperature. Large amount of reduction in κ_{ph} is measured for both high and low temperatures.

4.1.3. Graphene Coated Aluminium

Graphene layers are placed on top of the aluminium model to see its effect on κ_{ph}. For multilayer graphene, the thickness of the model is assumed the product of 0.34 (gap between two graphene layers) and number of graphene layers. Length dependency test is made for SLG and BLG coated aluminium. Figure 4.7 shows the κ_{ph} changing with the model length.

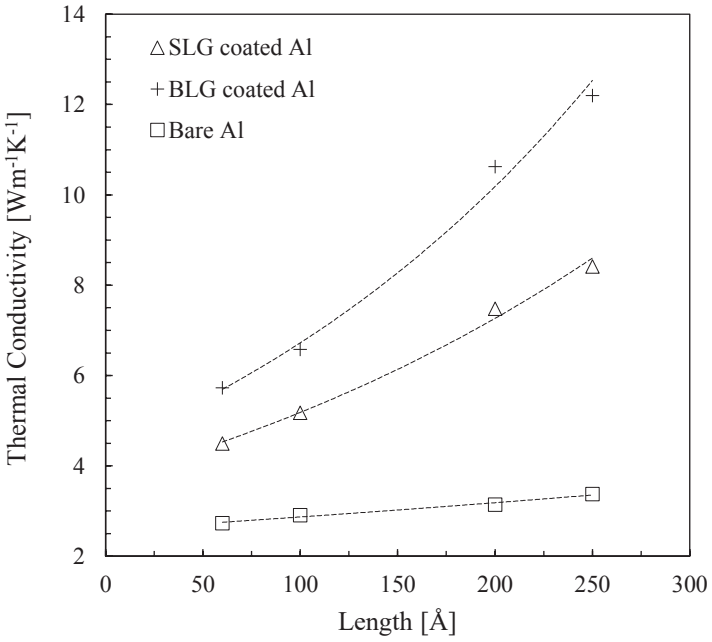

Figure 4.7 Length effect of thermal conductivity for aluminium, SLG coated aluminium and BLG coated aluminium

The κ_{ph} of all the models increases with the length. Also, a significant increase is achieved in κ_{ph} of aluminium with graphene coating. Maximum increase in κ_{ph} is achieved at 250 Å for both models. With SLG coating, κ_{ph} increased from 3.3 $Wm^{-1}K^{-1}$ to 8.4 $Wm^{-1}K^{-1}$. With BLG coating, κ_{ph} increased from 3.3 $Wm^{-1}K^{-1}$ to 12.2 $Wm^{-1}K^{-1}$. Increment ratios of 149% and 261% are achieved in κ_{ph} of aluminium with SLG and BLG coating respectively.

Beside SLG and BLG coatings, the effect of more layers is also investigated. Since aluminium block constitutes excessive number of atoms, the length dependency tests for these simulations requires too much computational power. For this reason, length

dependency test could not be conducted for number of graphene layers more than two. However, calculations are made with 60 Å length aluminium models to see the effect of more layers. Figure 4.8 shows the effect of graphene layer number on aluminium.

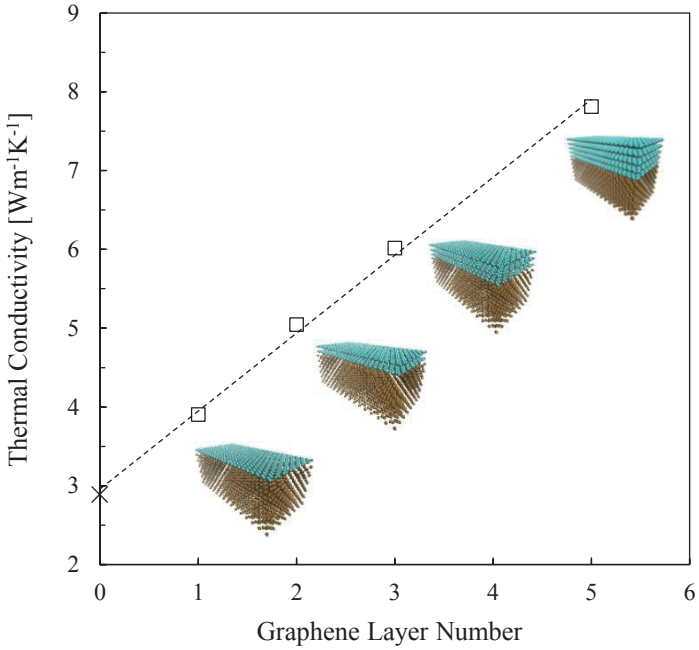

Figure 4.8 Graphene layer number effect on the thermal conductivity of 60 Å long aluminium

Figure 4.8 shows that κ_{ph} of aluminium block is highly affected by graphene coating. κ_{ph} of aluminium increases from 3 to 4 $Wm^{-1}K^{-1}$ with 1 layer of graphene coating and from 4 to 8 $Wm^{-1}K^{-1}$ with 5 layers of graphene coating which are 33% and 100% respectively. Since these simulations are made for a 60 Å long aluminium, with the help of information obtained from Figure 4.7 , it is expected that the rate of increase with graphene coating can be much higher for longer model lengths.

4.1.4. Defected Graphene

Thermal conductivity of defected graphene is calculated to understand the effect of defect size, shape and location. First, point defects are created for graphene. 25 different models with different number of point defects (from 10 to 50 atoms, 5 models for each) are created. In these models, defects are placed randomly by using a C++ code. Also, defects are placed in the main slab region to prevent the results effect from the heat

source and the heat sink. To obtain a mean thermal conductivity value 5 simulations are made for each case. Figure 4.9 shows the κ_{ph} change of point defected graphene with an increasing number of defected atoms.

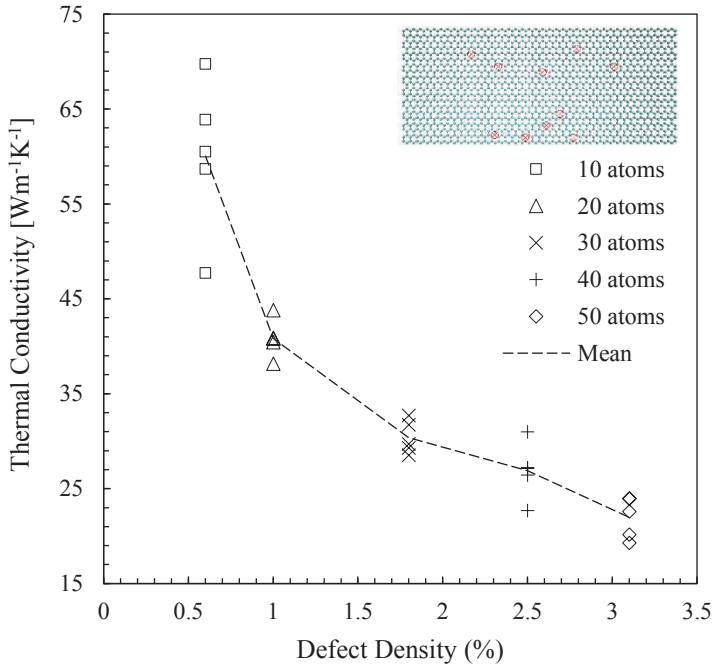

Figure 4.9 Effect of point defect density on thermal conductivity for SLG

From Figure 4.9, it can be seen that κ_{ph} of graphene is highly dependent on the number of point vacancy. κ_{ph} decreases sharply when the graphene layer becomes imperfect. It is also noticeable that the range of the results are wider for 1st case comparing to others. This is because, as the number of defects increases the probability of accumulating the defects in a certain area decreases. Thus, the mean value of 5 results is also given. κ_{ph} of SLG reduces from 127 $Wm^{-1}K^{-1}$ to 22 $Wm^{-1}K^{-1}$ as the defect density increases from 0.6% to 3.1%. For the first case (10-point vacancy), the results for κ_{ph} are in the range between 48-70 $Wm^{-1}K^{-1}$ and mean κ_{ph} is 60 $Wm^{-1}K^{-1}$. So, 0.6% defect density causes the κ_{ph} to drop 52%.

Secondly, line defects are created on SLG layer to investigate the effect of defect length on κ_{ph}. This is made for three different orientation: horizontal, vertical and crosswise. Crosswise defect is arranged diagonally. Atomistic models of these structures are shown in Figure 3.3. Figure 4.10 shows the comparison of defect line orientation on κ_{ph}.

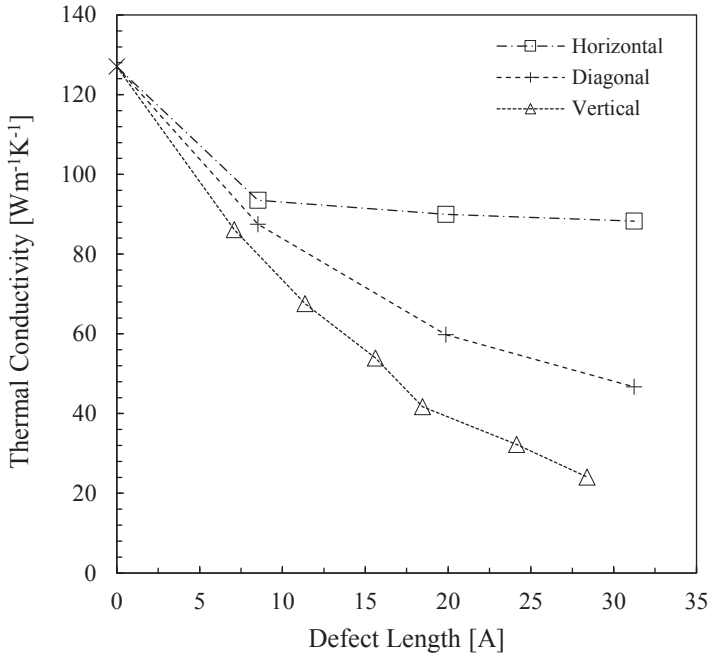

Figure 4.10 Effect of defect orientation and length on thermal conductivity of SLG

As shown in Figure 4.10, thermal conductivity decreases sharply as the defect length increases to ~10 Å for all defect orientations. At defect length of 10 Å, κ_{ph} decreases 29% from 127 $Wm^{-1}K^{-1}$ to ~90 $Wm^{-1}K^{-1}$. However, after 10 Å, there are significant differences in the reduction of thermal conductivity between 3 orientation. While reduction in κ_{ph} continues in crosswise and vertical defect lines, there is no change in κ_{ph} of the graphene with horizontal defect after 10 Å. Since horizontal defect is placed along the heat flow direction, it does not create a barrier on energy flow. So, it does not cause κ_{ph} to change. Furthermore, vertical defect created the maximum drop in κ_{ph} which is followed by diagonal defect. κ_{ph} decreased 81%, from 127 $Wm^{-1}K^{-1}$ to 24 $Wm^{-1}K^{-1}$ and 63%, from 127 $Wm^{-1}K^{-1}$ to 46 $Wm^{-1}K^{-1}$ with vertical and diagonal line defects respectively.

Finally, rectangular and circular shaped defects are simulated to investigate the effect of defect shape on thermal conductivity of SLG. Figure 4.11 shows the comparison of thermal conductivity of pristine SLG, rectangular and circular defected SLG.

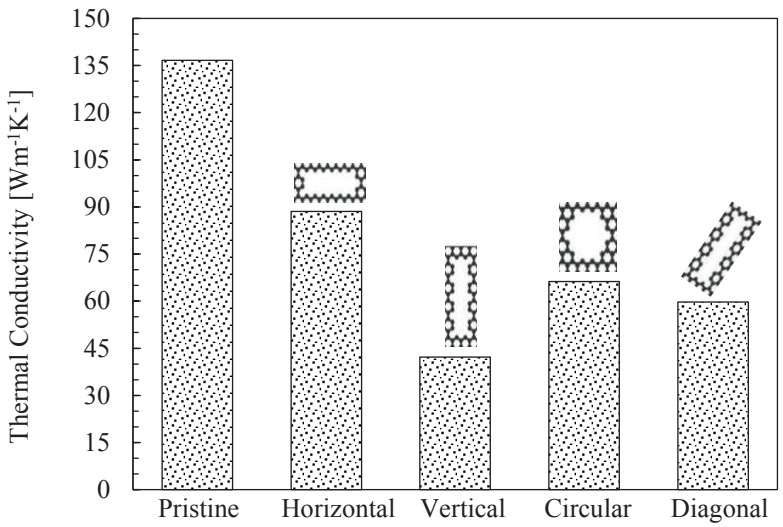

Figure 4.11 Comparison of thermal conductivities among SLG with different defect shapes

Figure 4.11 shows that κ_{ph} of graphene is directly related to the defect morphology. Even though the defect areas are arranged to be the same, there is a significant decrease in κ_{ph} when the defect is vertical. Results can be summarized as $\kappa_{ph,v} < \kappa_{ph,d} < \kappa_{ph,c} < \kappa_{ph,h}$. So, based on the information obtained from both Figure 4.10 and Figure 4.11, it can be inferred that the thermal conductivity is negatively related to the defect area perpendicular to the heat flow direction.

4.1.5. Defected Graphene Coated Aluminium

Effect of defects on thermal conductivity of graphene is investigated in Section 4.1.4. It is observed that even small number of defects can cause significant reduction in thermal conductivity. Defects may also occur on graphene during coating on aluminium. Defected graphene coated aluminium is also modeled and simulated to investigate the effects of defects in such case. For this case, 4 models are created. These models are randomly distributed point vacancy, horizontal, vertical and crosswise defects. Atomistic structures of these models are shown in Figure 3.3. Figure 4.12 shows the effect of point defect density on κ_{ph} of aluminium.

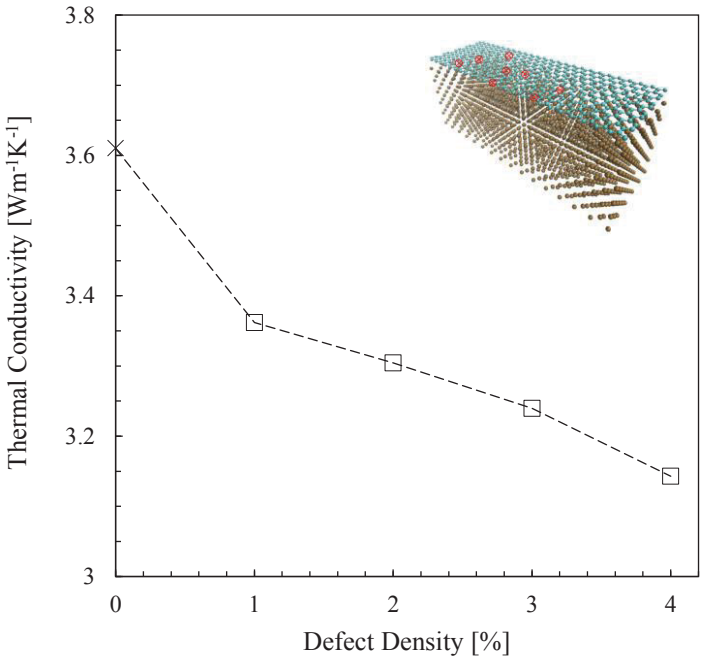

Figure 4.12 Thermal conductivity with increasing density of point vacancies on graphene coated aluminium

For the first case, 1% of point defect is created on graphene. κ_{ph} of graphene coated aluminium decreased 7% from 3.61 $Wm^{-1}K^{-1}$ to 3.36 $Wm^{-1}K^{-1}$. κ_{ph} decreases 13% from 3.61 $Wm^{-1}K^{-1}$ to 3.14 $Wm^{-1}K^{-1}$ as the defect density reaches to 4%. Comparing to SLG, the reduction in κ_{ph} is much smaller. This may be due to the smaller model dimensions used for graphene coated aluminium models for saving computational time. Also, the energy can flow through the aluminium block as it faces the vacancies so that the defects on graphene does not affect the κ_{ph} significantly.

Defect orientation is also investigated as it was done for SLG. For this, vertical, horizontal and diagonal defect are created on graphene layer which is then placed on aluminium block. Atomistic structures of these models are given in Figure 3.3. Defect length dependency of the κ_{ph} of graphene coated aluminium is shown in Figure 4.13.

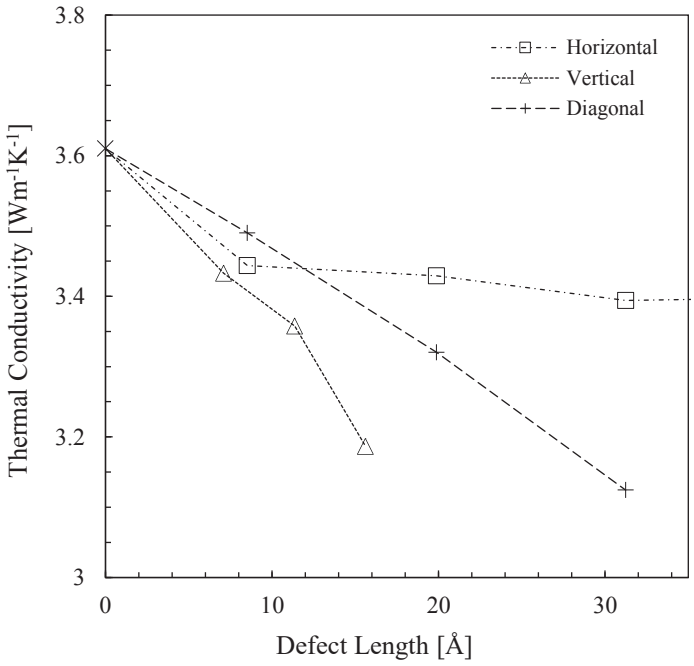

Figure 4.13 Defect orientation and length effects on thermal conductivity for graphene-coated aluminium

Figure 4.13 shows that κ_{ph} decreases as the defect length increases. Similar to SLG case, tendency difference in κ_{ph} starts at ~8 Å. After 10 Å, for the horizontal orientation, κ_{ph} changes slightly. However, there is a significant drop in κ_{ph} for vertical and diagonal orientations. For ~20 Å defect length, the κ_{ph} decreases 12% and 7.7% for vertical and diagonal defects respectively.

4.2. Experimental Results

Two different cases are investigated with the experimental setup. 0.5wt.%GNP reinforced and non-reinforced A360 aluminium samples are heated up to see the effect of graphene on temperature distribution and heat transfer to the air. Figure 4.14 summarizes the results for 2 experiments conducted to see the change of ΔT with the airspeed. In Figure 4.14, the x-axis is the mean airspeed and the y-axis is the absolute temperature difference between the inlet and the outlet.

In Figure 4.14, it is shown that GNP reinforced sample has lower performance than Al360 sample. For all the airspeed cases, the mean difference in ΔT is calculated as 10%. It is estimated that these differences arise from various reasons such as sample production, GNP orientation, and GNP structure.

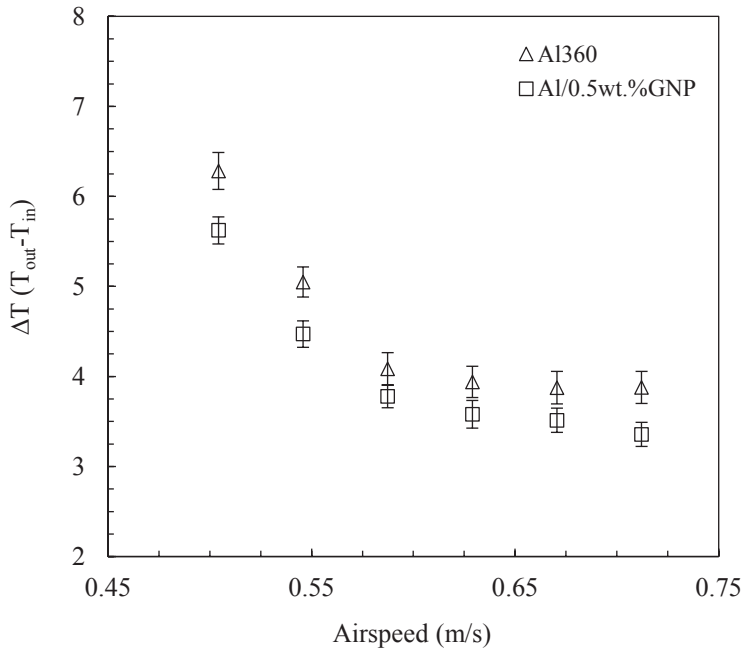

Figure 4.14 Air speed vs. inlet-outlet temperature difference for comparison of 0.5wt.%GNP reinforced and non-reinforced Al samples

Firstly, it may be caused by porosities that may have occurred inside AMMC during casting. Porosities might be blocking the heat transport across the sample and lead to a low thermal performance comparing to Al360 sample. Moreover, graphene's through-plane thermal conductivity is much lower than its in-plane thermal conductivity (Chu et al. 2018). Hence, graphene orientation is also important for the thermal transport. In GNP reinforced sample, GNPs are not aligned in heat flow direction. Since the reinforced sample is produced with stirring and casting, some of the GNP particles will be angled with the heat flow direction. It is shown that graphene alignment is important on thermal transport across the sample (Malekpour et al. 2014). Besides, since graphene is not in a continuous structure in the material, it may not have much effect on thermal conduction.

CHAPTER 5

CONCLUSION

Thermal conductivity of graphene and aluminum is simulated with the NEMD code written in C++ programming language. Thermal conductivity of these models is compared with reference works and shown that the results are consistent with the literature.

The effect of graphene coating on aluminium is investigated. SLG and BLG coated aluminium models are investigated with increasing lengths. It is shown that the thermal conductivity increases as the length increases. Besides, graphene coating causes a significant increase in the thermal conductivity of aluminum. Aluminum with graphene up to five layers is modeled and the effect of layer number on thermal conductivity is investigated. It is found that, thermal conductivity increases linearly as the layer number increases.

Defected models are studied to investigate the effects of defects on both graphene and graphene-coated aluminium. Point defects and line defects are created on the surface of graphene layer. It was shown that thermal conductivity of SLG is strongly dependent on the number of point defects. The thermal conductivity of graphene decreases drastically as the point defect number increases. Moreover, the effect of the length of horizontal, vertical and diagonal line defects are studied. It is shown that the highest drop in thermal conductivity occurs in vertical oriented defects followed by the diagonal and horizontal defects, for the same lengths. Thermal conductivity decreases drastically for the vertical and diagonal defect cases. However, thermal conductivity does not change after a certain point. It is found that thermal conductivity is highly dependent on the defect projection perpendicular to the heat flow direction. Similar results are also observed with the graphene coated aluminium model.

In the experimental part, thermal performance of 0.5wt.% GNP reinforced Al and Al360 is investigated and compared. GNP reinforced sample showed a lower thermal performance comparing to Al sample. This founding is associated with the graphene orientation and porosity build-up during the production stages. However, Al reinforced

samples with higher GNP ratios with GNPs oriented in the heat flow direction can be tested and analyzed as a future work.

Finally, numerical results showed that graphene is a promising coating material on aluminium for thermal applications. However, thermal conductivity is strongly dependent on the defect size and orientation. Hence, the production process of graphene-coated aluminum is of great importance in order to achieve high thermal conductivity values.

As a future work, graphene layers can be placed inside of the aluminium block to model GNP reinforced aluminium. Also, the effect of defects on aluminium on thermal conductivity can be investigated.

APPENDICIES

APPENDIX A

TECHNICAL DRAWINGS OF SAMPLE HOLDER

All dimensions are in mm.

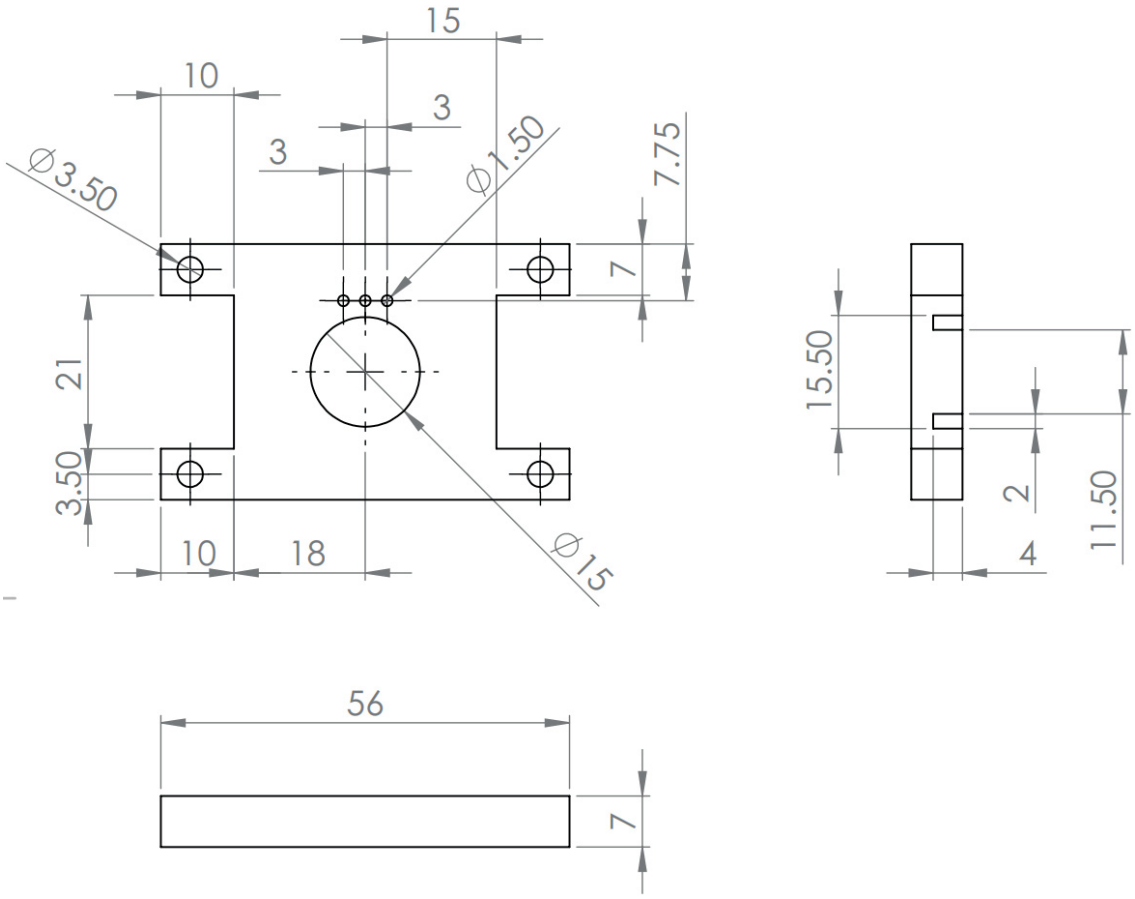

Figure A.1 Technical drawing of bottom part of the sample holder

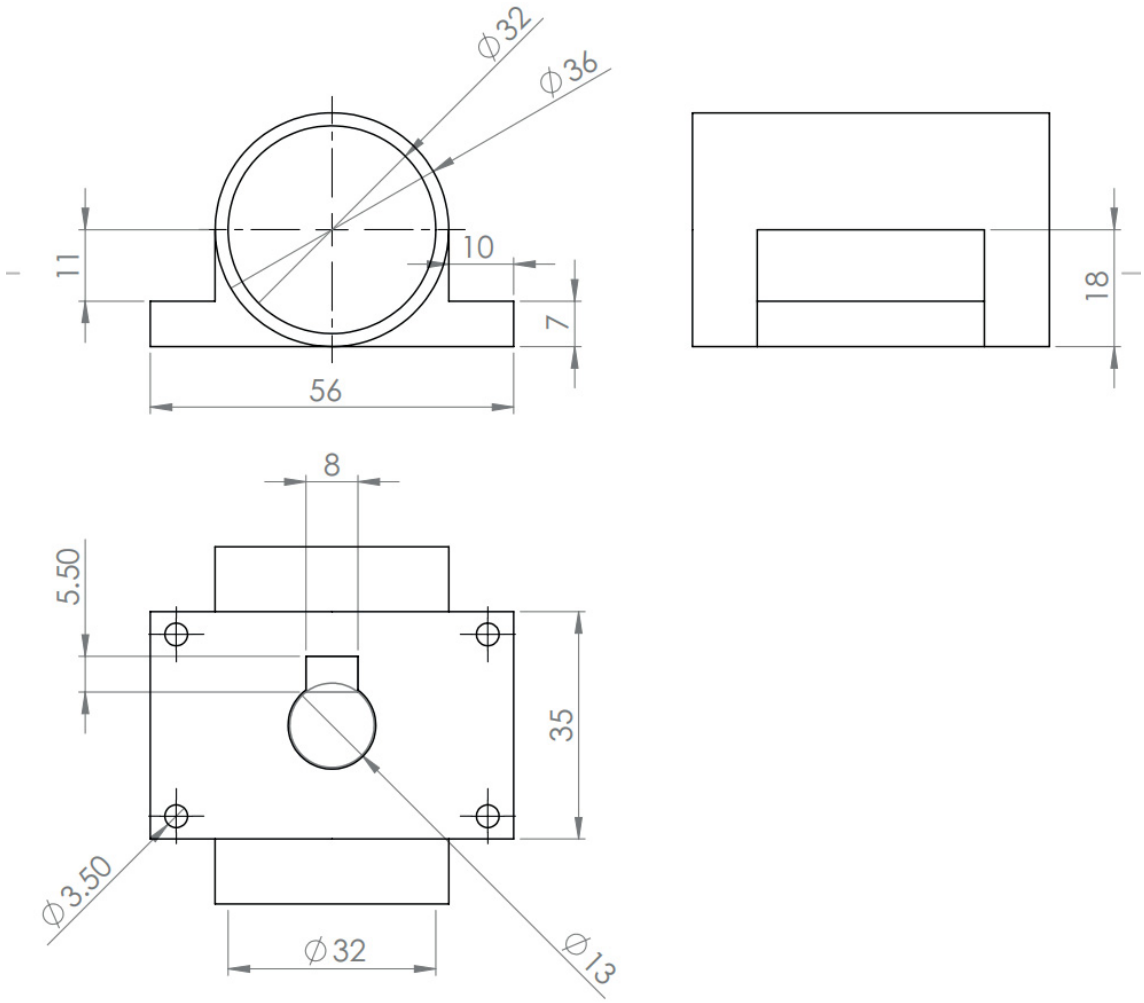

Figure A.2 Technical drawing of upper part of the sample holder

APPENDIX B

C++ ALGORITHMS FOR INTERATOMIC POTENTIALS

Lennard Jones Potential code for Al-C interactions:

```
void Lennard_Jones_AlC() {

	for (i = start_al[myrank]; i < end_al[myrank]; i++) {

		for (j = 0; j < NC; j++) {

			dist = sqrt(pow((post_al[i].x - post_c[j].x), 2.0) +
			pow((post_al[i].y - post_c[j].y), 2.0) + pow((post_al[i].z -
			post_c[j].z), 2.0));

			if (dist < critic_lj) {
				double sd = sigma / dist;

				force = (((48.0 * eps) / (pow(sigma, 2.0)))*(pow((sd),
				14.0) - (0.5)*pow((sd), 8.0))-trunc1)*dist;

				distd = 1.0 / dist;

				fx = (force * (post_al[i].x - post_c[j].x) * distd);
				fy = (force * (post_al[i].y - post_c[j].y) * distd);
				fz = (force * (post_al[i].z - post_c[j].z) * distd);

				frc_al[i].i = frc_al[i].i + fx;
				frc_al[i].j = frc_al[i].j + fy;
				frc_al[i].k = frc_al[i].k + fz;

				frc_c[j].i = frc_c[j].i - fx;
				frc_c[j].j = frc_c[j].j - fy;
				frc_c[j].k = frc_c[j].k - fz;
			}
		}
	}
}
```

Sutton-Chen Potential code for Al-Al interactions:

```
void Sutton_Chen() {
	for (i1 = 0; i1 < NAl; i1++) {
		rho[i1] = 0.0;
	}
	for (i = start_al[myrank]; i < end_al[myrank]; i++) {
		for (j = i + 1; j < NAl; j++) {
			dist = sqrt(pow((post_al[i].x - post_al[j].x), 2.0) +
			pow((post_al[i].y - post_al[j].y), 2.0) + pow((post_al[i].z -
			post_al[j].z), 2.0));
			if (dist < critic_s) {
				double stbin1 = pow((sigma_s / dist), m_s);
				rho[i] = rho[i] + stbin1;
				rho[j] = rho[j] + stbin1;
			}
		}
	}

	MPI_Barrier(MPI_COMM_WORLD);
	MPI_Allreduce(MPI_IN_PLACE, &rho[0], NAl, MPI_DOUBLE, MPI_SUM,
	MPI_COMM_WORLD);
	MPI_Barrier(MPI_COMM_WORLD);

	for (i = start_al[myrank]; i < end_al[myrank]; i++) {
		for (j = i + 1; j < NAl; j++) {

			dist = sqrt(pow((post_al[i].x - post_al[j].x), 2.0) +
			pow((post_al[i].y - post_al[j].y), 2.0) + pow((post_al[i].z -
			post_al[j].z), 2.0));
			distd = 1.0 / dist;
			sd = sigma_s / dist;

			if (dist < critic_s) {

				pot_met[i] = pot_met[i] + eps_s * 0.5*pow(sd, n_s) -
				c_s * sqrt(rho[i]);
				pot_met[j] = pot_met[j] + eps_s * 0.5*pow(sd, n_s) -
				c_s * sqrt(rho[j]);

				force_s = eps_s * ((n_s*pow((sd), n_s)) -
				((c_s*m_s*0.5)*((1 / (pow(rho[i], 0.5))) + (1 /
				pow(rho[j], 0.5)))*(pow((sd), m_s)))) * (distd);

				fx = (force_s * (post_al[i].x - post_al[j].x) *
				distd);
				fy = (force_s * (post_al[i].y - post_al[j].y) *
				distd);
				fz = (force_s * (post_al[i].z - post_al[j].z) *
				distd);

				frc_al[i].i = frc_al[i].i + fx;
				frc_al[i].j = frc_al[i].j + fy;
				frc_al[i].k = frc_al[i].k + fz;

				frc_al[j].i = frc_al[j].i - fx;
				frc_al[j].j = frc_al[j].j - fy;
				frc_al[j].k = frc_al[j].k - fz;
			}
		}
	}
}
```

Tersoff Potential code for C-C interactions:

```
void Tersoff() {

	for (i = start_c[myrank]; i < end_c[myrank]; i++) {
		for (int j1 = 1; j1 < 4; j1++) {

			int j = neighbors[i][j1];
			if (j != -1) {
				t1 = post_c[i].x - post_c[j].x;
				t2 = post_c[i].y - post_c[j].y;
				t3 = post_c[i].z - post_c[j].z;

				rij = sqrt(t1 * t1 + t2 * t2 + t3 * t3);

				tij_i = t1 / rij;
				tij_j = t2 / rij;
				tij_k = t3 / rij;

				vaij = A * exp(-lamda1 * rij);
				vrij = B * exp(-lamda2 * rij);

				if (rij < R) {
					fcij = 1.0;
					dfcij = 0.0;
				}
				else if (rij > S) {
					fcij = 0.0;
					dfcij = 0.0;
				}
				else {
					argij = M_PI * ((rij - R) / (S - R));
					fcij = 0.5*(1.0 + cos(argij));
					dfcij = -0.5*M_PI*sin(argij) / (S - R);
				}
				epsij = 0.0;
				for (int l1 = 1; l1 < 4; l1++) {

					int l = neighbors[i][l1];

					if (l != -1 && l != j) {

						t1 = post_c[i].x - post_c[l].x;
						t2 = post_c[i].y - post_c[l].y;
						t3 = post_c[i].z - post_c[l].z;

						rik = sqrt(t1 * t1 + t2 * t2 + t3 * t3);

						tik_i = t1 / rik;
						tik_j = t2 / rik;
						tik_k = t3 / rik;
						if (rik < R) {
							fcik = 1.0;
						}
						else if (rik > S) {
							fcik = 0.0;
						}
						else {
							argik = M_PI * ((rik - R) / (S -
							R));
							fcik = 0.5*(1.0 + cos(argik));
```

```
                }

                cost = tij_i * tik_i + tij_j * tik_j +
                tij_k * tik_k;
                gtheta = 1.0 + ((c*c) / (d*d)) - (c * c)
                / (d * d + ((h - cost) * (h - cost)));
                epsij = epsij + fcik * gtheta;
        }
}

temp1 = beta * epsij;
if (temp1 < 0.0) {
        temp2 = 1.0;
        bij = 1.0;
        coef1 = 0.0;
}
else {
        temp2 = 1.0 + pow(temp1, n);
        bij = pow(temp2, n3);
        coef1 = 0.5*beta*pow(temp1, n1)*pow(temp2,
        n2)*fcij*vrij;
}

pot_car[i] = fcij * (vaij - bij * vrij);

fij = -0.5*(vaij*(dfcij - fcij * lamda1) - bij *
vrij*(dfcij - fcij * lamda2));

fij_x = fij * tij_i;
fij_y = fij * tij_j;
fij_z = fij * tij_k;

frc_c[i].i = frc_c[i].i + fij_x;
frc_c[i].j = frc_c[i].j + fij_y;
frc_c[i].k = frc_c[i].k + fij_z;

frc_c[j].i = frc_c[j].i - fij_x;
frc_c[j].j = frc_c[j].j - fij_y;
frc_c[j].k = frc_c[j].k - fij_z;

for (int k1 = 1; k1 < 4; k1++) {

        int k = neighbors[i][k1];
        if (k != -1 && k != j) {

                t1 = post_c[i].x - post_c[k].x;
                t2 = post_c[i].y - post_c[k].y;
                t3 = post_c[i].z - post_c[k].z;

                rik = sqrt(t1 * t1 + t2 * t2 + t3 * t3);

                tik_i = t1 / rik;
                tik_j = t2 / rik;
                tik_k = t3 / rik;

                if (rik < R) {
                        fcik = 1.0;
                        dfcik = 0.0;
                }
                else if (rik > S) {
                        fcik = 0.0;
                        dfcik = 0.0;
```

```
                                        }
                                        else {
                                               argik = M_PI * (rik - R) / (S -
                                               R);
                                               fcik = 0.5*(1.0 + cos(argik));
                                               dfcik = -0.5*M_PI*sin(argik) / (S
                                               - R);
                                        }
                                        cost = tij_i * tik_i + tij_j * tik_j +
                                        tij_k * tik_k;
                                        a = (d * d) + ((h - cost) * (h - cost));
                                        gtheta = 1.0 + ((c*c) / (d*d)) - (c * c)
                                        / a;
                                        coef2 = -fcik * 2.0*c*c*(h - cost) /
                                        pow(a, 2.0);

                                        fk_x = 0.5*coef1*(gtheta * dfcik * tik_i
                                        + coef2 * (tij_i - cost * tik_i) / rik);
                                        fk_y = 0.5*coef1*(gtheta * dfcik * tik_j
                                        + coef2 * (tij_j - cost * tik_j) / rik);
                                        fk_z = 0.5*coef1*(gtheta * dfcik * tik_k
                                        + coef2 * (tij_k - cost * tik_k) / rik);

                                        fj_x = 0.5*coef1*coef2*(tik_i - cost *
                                        tij_i) / rij;
                                        fj_y = 0.5*coef1*coef2*(tik_j - cost *
                                        tij_j) / rij;
                                        fj_z = 0.5*coef1*coef2*(tik_k - cost *
                                        tij_k) / rij;

                                        frc_c[i].i = frc_c[i].i - (fk_x + fj_x);
                                        frc_c[i].j = frc_c[i].j - (fk_y + fj_y);
                                        frc_c[i].k = frc_c[i].k - (fk_z + fj_z);

                                        frc_c[j].i = frc_c[j].i + fj_x;
                                        frc_c[j].j = frc_c[j].j + fj_y;
                                        frc_c[j].k = frc_c[j].k + fj_z;

                                        frc_c[k].i = frc_c[k].i + fk_x;
                                        frc_c[k].j = frc_c[k].j + fk_y;
                                        frc_c[k].k = frc_c[k].k + fk_z;

                                }
                        }
                }
        }
}
```

APPENDIX C

FAN CHARACTERISTICS

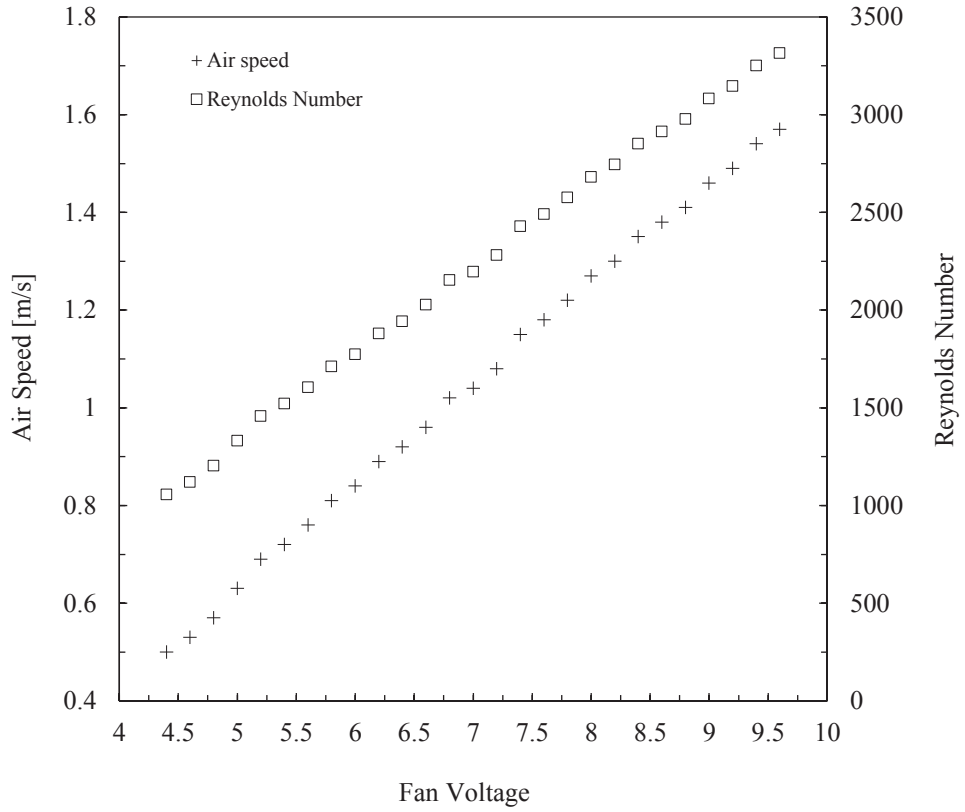

Figure C.1 Fan voltage vs. outlet air speed and Reynolds number

REFERENCES

Abhinav, Ch, K Vamsi Krishna Reddy, G Goutham Raju, and K Subramanyam. 2017. "Experimental Investigation of Graphene Coated Al Cuboid Crammed with PCM ` s for Efficient Thermal Energy Storage and Conversion .," 396–402.

Baimova, J. A., Liu Bo, S. V. Dmitriev, K. Zhou, and A. A. Nazarov. 2013. "Effect of Stone-Thrower-Wales Defect on Structural Stability of Graphene at Zero and Finite Temperatures." *EPL* 103 (4). doi:10.1209/0295-5075/103/46001.

Balandin, Alexander A, Suchismita Ghosh, Wenzhong Bao, Irene Calizo, Desalegne Teweldebrhan, Feng Miao, and Chun Ning Lau. 2008. "Superior Thermal Conductivity of Single-Layer Graphene." *Nano Letters* 8 (3): 902–7. doi:10.1021/nl0731872.

Bolotin, K. I., K. J. Sikes, Z. Jiang, M. Klima, G. Fudenberg, J. Hone, P. Kim, and H. L. Stormer. 2008. "Ultrahigh Electron Mobility in Suspended Graphene." *Solid State Communications* 146 (9–10): 351–55. doi:10.1016/j.ssc.2008.02.024.

Cao, Ajing. 2012. "Molecular Dynamics Simulation Study on Heat Transport in Monolayer Graphene Sheet with Various Geometries." *Journal of Applied Physics* 111 (8): 83528. doi:10.1063/1.4705510.

Chantrenne, Raynaud, and Barrat. 2003a. "STUDY OF PHONON HEAT TRANSFER IN METALLIC SOLIDS FROM MOLECULAR DYNAMIC SIMULATIONS." *Microscale Thermophysical Engineering* 7 (2): 117–36. doi:10.1080/10893950390203314.

Cho, Hyunjin, Hokyun Rho, Jun Hee Kim, Su Hyeong Chae, Thang Viet Pham, Tae Hoon Seo, Hak Yong Kim, et al. 2017. "Graphene-Carbon-Metal Composite Film for a Flexible Heat Sink." *ACS Applied Materials and Interfaces* 9 (46). American Chemical Society: 40801–9. doi:10.1021/acsami.7b11485.

Chu, Ke, Xiao-hu Wang, Yu-biao Li, Da-jian Huang, Zhong-rong Geng, Xi-long Zhao, Hong Liu, and Hu Zhang. 2018. "Thermal Properties of Graphene/Metal Composites with Aligned Graphene." *Materials & Design* 140 (February): 85–94.

doi:10.1016/j.matdes.2017.11.048.

Deyirmenjian, V B, V Heine, M C Payne, V. Milman, R. M. Lynden-Bell, and M. W. Finnis. 1995. “Ab Initio Atomistic Simulation of the Strength of Defective Aluminum and Tests of Empirical Force Models.” *Physical Review B* 52 (21): 15191–207. doi:10.1103/PhysRevB.52.15191.

Edwards, Rebecca S., and Karl S. Coleman. 2013. “Graphene Synthesis: Relationship to Applications.” *Nanoscale* 5 (1). The Royal Society of Chemistry: 38–51. doi:10.1039/c2nr32629a.

Erturk, Ahmet Semih, Mesut Kirca, and Levent Kirkayak. 2018. “Mechanical Enhancement of an Aluminum Layer by Graphene Coating.” *Journal of Materials Research* 33 (18): 2741–51. doi:10.1557/jmr.2018.261.

Fang, Xin, Li Wu Fan, Qing Ding, Xiao Wang, Xiao Li Yao, Jian Feng Hou, Zi Tao Yu, Guan Hua Cheng, Ya Cai Hu, and Ke Fa Cen. 2013. “Increased Thermal Conductivity of Eicosane-Based Composite Phase Change Materials in the Presence of Graphene Nanoplatelets.” *Energy and Fuels* 27 (7). American Chemical Society: 4041–47. doi:10.1021/ef400702a.

Feng, Tianli, Xiulin Ruan, Zhenqiang Ye, and Bingyang Cao. 2015. “Spectral Phonon Mean Free Path and Thermal Conductivity Accumulation in Defected Graphene: The Effects of Defect Type and Concentration.” *PHYSICAL REVIEW B* 91: 224301. doi:10.1103/PhysRevB.91.224301.

Filippova, V P, S A Kunavin, and M S Pugachev. 2015. “Calculation of the Parameters of the Lennard-Jones Potential for Pairs of Identical Atoms Based on the Properties of Solid Substances.” *Inorganic Materials: Applied Research* 6 (1): 1–4. doi:10.1134/s2075113315010062.

Ghosh, S, I Calizo, D Teweldebrhan, E P Pokatilov, D L Nika, A A Balandin, W Bao, F Miao, and C N Lau. 2008. “Extremely High Thermal Conductivity of Graphene: Prospects for Thermal Management Applications in Nanoelectronic Circuits.” *Applied Physics Letters* 92 (15): 151911. doi:10.1063/1.2907977.

Gropp, W, WD Gropp, E Lusk, A Skjellum, and ADFEE Lusk. 1999. “Using MPI:

Portable Parallel Programming with the Message-Passing Interface." https://www.google.com/books?hl=tr&lr=&id=xpBZ0RyRb-oC&oi=fnd&pg=PA1&dq=%22Using+MPI%22,+Gropp,+Lusk+and+Skjellum.+MIT+Press,+1994.&ots=ud9yj0NO9Z&sig=tN24KeYr7zvlwUJ9aPud8JxGMDs.

Han, Xiaopeng, Ying Huang, Qiao Gao, Meng Yu, and Xuefang Chen. 2018. "High Thermal Conductivity and Mechanical Properties of Nanotube@Cu/Ag@Graphite/Aluminum Composites." *Industrial & Engineering Chemistry Research* 57 (31): 10365–71. doi:10.1021/acs.iecr.8b01567.

Hsieh, Chien Te, Yu Fu Chen, Cheng En Lee, Yu Ming Chiang, Keng Yen Hsieh, and Ho Sheng Wu. 2017. "Heat Transport Enhancement of Heat Sinks Using Cu-Coated Graphene Composites." *Materials Chemistry and Physics* 197 (August). Elsevier Ltd: 105–12. doi:10.1016/j.matchemphys.2017.05.012.

Huang, Yu, Qiubao Ouyang, Qiang Guo, Xingwu Guo, Guoding Zhang, and Di Zhang. 2016. "Graphite Film/Aluminum Laminate Composites with Ultrahigh Thermal Conductivity for Thermal Management Applications." *Materials & Design* 90 (January): 508–15. doi:10.1016/j.matdes.2015.10.146.

Jain, Ankit, and Alan J H McGaughey. 2016. "Thermal Transport by Phonons and Electrons in Aluminum, Silver, and Gold from First Principles." *Physical Review B* 93 (8): 81206. doi:10.1103/PhysRevB.93.081206.

Jeon, Chi Hoon, Yong Ha Jeong, Jeong Jin Seo, Huynh Ngoc Tien, Sung Tae Hong, Young Jin Yum, Seung Hyun Hur, and Kwang Jin Lee. 2014. "Material Properties of Graphene/Aluminum Metal Matrix Composites Fabricated by Friction Stir Processing." *International Journal of Precision Engineering and Manufacturing* 15 (6): 1235–39. doi:10.1007/s12541-014-0462-2.

Kimura, Yoshitaka, Yue Qi, Tahir C Ggn, and William A Goddard III. 1998. "The Quantum Sutton-Chen Many-Body Potential for Properties of Fcc Metals." *Materials and Process Simulation Center*. http://citeseerx.ist.psu.edu/viewdoc/download;jsessionid=EA20ED3DC4B6912412BA8A58729AF416?doi=10.1.1.26.3890&rep=rep1&type=pdf.

Kousalya, Arun S., Anurag Kumar, Rajib Paul, Dmitry Zemlyanov, and Timothy S.

Fisher. 2013. “Graphene: An Effective Oxidation Barrier Coating for Liquid and Two-Phase Cooling Systems.” *Corrosion Science*. Pergamon. doi:10.1016/j.corsci.2012.12.014.

Kuang, Da, Liye Xu, Lei Liu, Wenbin Hu, and Yating Wu. 2013. “Graphene-Nickel Composites.” *Applied Surface Science* 273 (May). Elsevier B.V.: 484–90. doi:10.1016/j.apsusc.2013.02.066.

Kumar, Sunil. 2017. “Graphene Engendered 2-D Structural Morphology of Aluminium Atoms: Molecular Dynamics Simulation Study.” *Materials Chemistry and Physics* 202 (December). Elsevier: 329–39. doi:10.1016/j.matchemphys.2017.09.043.

Lee, Changgu, Xiaoding Wei, Jeffrey W Kysar, and James Hone. 2008a. “Measurement of the Elastic Properties and Intrinsic Strength of Monolayer Graphene.” *Science* 321 (5887). American Association for the Advancement of Science: 385–88. doi:10.1126/science.1157996.

Lei, Yinxiang, Yuping Yan, and Jiajiang Lv. 2019. “Atomistic Study of the Strengthening Mechanisms of Graphene Coated Aluminum.” doi:10.1088/1361-6528/ab4952.

Liem, Steven Y, and Kwong Yu Chan. 1995. “Simulation Study of Platinum Adsorption on Graphite Using the Sutton-Chen Potential.” *Surface Science* 328 (1–2): 119–28. doi:10.1016/0039-6028(95)00016-X.

Liu, Jianhua, Lei Hua, Songmei Li, and Mei Yu. 2015. “Graphene Dip Coatings: An Effective Anticorrosion Barrier on Aluminum.” *Applied Surface Science* 327 (February). North-Holland: 241–45. doi:10.1016/j.apsusc.2014.11.187.

Liu, Jinghang, Umar Khan, Jonathan Coleman, Bea Fernandez, Pablo Rodriguez, Sumsun Naher, and Dermot Brabazon. 2016. “Graphene Oxide and Graphene Nanosheet Reinforced Aluminium Matrix Composites: Powder Synthesis and Prepared Composite Characteristics.” *Materials & Design* 94 (March). Elsevier: 87–94. doi:10.1016/j.matdes.2016.01.031.

Liu, Xiao, Thomas H. Metcalf, Jeremy T. Robinson, Brian H. Houston, and Fabrizio Scarpa. 2012. “Shear Modulus of Monolayer Graphene Prepared by Chemical Vapor Deposition.” *Nano Letters* 12 (2). Nano Lett: 1013–17. doi:10.1021/nl204196v.

Malekpour, H, K.-H Chang, J.-C Chen, C.-Y Lu, D L Nika, K S Novoselov, and A A Balandin. 2014. “Thermal Conductivity of Graphene Laminate.” *Nano Lett* 14. doi:10.1021/nl501996v.

Martin, Seçkin, Sinan Kandemir, and Maksim Antonov. 2020. “Investigation of the High Temperature Dry Sliding Wear Behavior of Graphene Nanoplatelets Reinforced Aluminum Matrix Composites.” *Journal of Composite Materials*. doi:10.1177/0021998320979037.

Matsubara, Hiroki, Gota Kikugawa, Takeshi Bessho, Seiji Yamashita, and Taku Ohara. 2016. “Non-Equilibrium Molecular Dynamics Simulation as a Method of Calculating Thermodynamic Coefficients.” *Fluid Phase Equilibria* 421 (August). Elsevier: 1–8. doi:10.1016/j.fluid.2016.03.019.

Mohan, Velram Balaji, Kin tak Lau, David Hui, and Debes Bhattacharyya. 2018. “Graphene-Based Materials and Their Composites: A Review on Production, Applications and Product Limitations.” *Composites Part B: Engineering*. Elsevier Ltd. doi:10.1016/j.compositesb.2018.01.013.

Mortazavi, Bohayra, and Saïd Ahzi. 2013. “Thermal Conductivity and Tensile Response of Defective Graphene: A Molecular Dynamics Study.” *Carbon* 63: 460–70. doi:10.1016/j.carbon.2013.07.017.

Nosé, Shuichi. 1984. “A Unified Formulation of the Constant Temperature Molecular Dynamics Methods.” *The Journal of Chemical Physics* 81 (1): 511–19. doi:10.1063/1.447334.

Novoselov, K S, D Jiang, F Schedin, T J Booth, V V Khotkevich, S V Morozov, and A K Geim. 2005. “Two-Dimensional Atomic Crystals.” *Proceedings of the National Academy of Sciences of the United States of America* 102 (30). National Academy of Sciences: 10451–53. doi:10.1073/pnas.0502848102.

Porwal, H., S. Grasso, and M. J. Reece. 2013. “Review of Graphene-Ceramic Matrix Composites.” *Advances in Applied Ceramics*. Taylor & Francis. doi:10.1179/174367613X13764308970581.

Rajabpour, A., and S. M. Vaez Allaei. 2012. “Tuning Thermal Conductivity of Bilayer

Graphene by Inter-Layer s p 3 Bonding: A Molecular Dynamics Study." *Applied Physics Letters* 101 (5): 1–5. doi:10.1063/1.4740259.

Rajasekaran, G, Rajesh Kumar, and Avinash Parashar. 2016a. "Tersoff Potential with Improved Accuracy for Simulating Graphene in Molecular Dynamics Environment." *Materials Research Express* 3 (3). IOP Publishing: 35011. doi:10.1088/2053-1591/3/3/035011.

Saboori, Abdollah, Matteo Pavese, Claudio Badini, and Paolo Fino. 2017. "Microstructure and Thermal Conductivity of Al-Graphene Composites Fabricated by Powder Metallurgy and Hot Rolling Techniques." *Acta Metallurgica Sinica (English Letters)* 30 (7). Chinese Society for Metals: 675–87. doi:10.1007/s40195-017-0579-2.

Sharma, Sumit, Pramod Kumar, and Rakesh Chandra. 2017. "Mechanical and Thermal Properties of Graphene–Carbon Nanotube-Reinforced Metal Matrix Composites: A Molecular Dynamics Study." *Journal of Composite Materials* 51 (23): 3299–3313. doi:10.1177/0021998316682363.

Sharma, Sumit, Pramod Kumar, Navin Kumar, and Rakesh Chandra. 2018. "Graphene/Carbon Nanotube-Reinforced Nickel Composites: A Molecular Dynamics Study." *Composites: Mechanics, Computations, Applications* 9 (3). Begell House Inc.: 247–68. doi:10.1615/CompMechComputApplIntJ.2018021097.

Shin, S. E., H. J. Choi, J. H. Shin, and D. H. Bae. 2015. "Strengthening Behavior of Few-Layered Graphene/Aluminum Composites." *Carbon* 82 (C). Elsevier Ltd: 143–51. doi:10.1016/j.carbon.2014.10.044.

Sidorenkov, A V, S V Kolesnikov, and A M Saletsky. 2016. "Molecular Dynamics Simulation of Graphene on Cu(111) with Different Lennard-Jones Parameters," no. 111.

Su, Ruixia, and Xing Zhang. 2018. "Size Effect of Thermal Conductivity in Monolayer Graphene." *Applied Thermal Engineering* 144 (November). Pergamon: 488–94. doi:10.1016/j.applthermaleng.2018.08.062.

Sutton, A. P., and J. Chen. 1990. "Long-Range Finnis-Sinclair Potentials." *Philosophical*

Magazine Letters 61 (3): 139–46. doi:10.1080/09500839008206493.

Tersoff, J. 1988. "New Empirical Approach for the Structure and Energy of Covalent Systems." *Physical Review B* 37 (12): 6991–7000. doi:10.1103/PhysRevB.37.6991.

Verlet, Loup. 1967. "Computer 'Exyeriments' on Classical Fluids. I. Thermodynamical Properties of Lennard-Jones Molecules." *Physical Review* 159 (2): 183–95. doi:10.1088/0022-3727/9/2/008.

Wang, Yan, Zexi Lu, and Xiulin Ruan. 2016. "First Principles Calculation of Lattice Thermal Conductivity of Metals Considering Phonon-Phonon and Phonon-Electron Scattering." *Journal of Applied Physics* 119 (22): 225109. doi:10.1063/1.4953366.

Wei, Zhiyong, Zhonghua Ni, Kedong Bi, Minhua Chen, and Yunfei Chen. 2011a. "In-Plane Lattice Thermal Conductivities of Multilayer Graphene Films." *Carbon* 49 (8). Elsevier Ltd: 2653–58. doi:10.1016/j.carbon.2011.02.051.

Yan, Shao Jiu, Cheng Yang, Qi Hu Hong, Jun Zhou Chen, Da Bo Liu, and Sheng Long Dai. 2014. "Research of Graphene-Reinforced Aluminum Matrix Nanocomposites." *Cailiao Gongcheng/Journal of Materials Engineering*, no. 4. Beijing Institute of Aeronautical Materials (BIAM): 1–6. doi:10.3969/j.issn.1001-4381.2014.04.001.

Zhan, Niwei, Bo Chen, Changzheng Li, and Pei Kang Shen. 2018. "Molecular Dynamics Simulations of the Thermal Conductivity of Graphene for Application in Wearable Devices Recent Citations Molecular Dynamics Simulations of the Thermal Conductivity of Graphene for Application in Wearable Devices." doi:10.1088/1361-6528/aae98b.

Zhang, Le, Guangmei Hou, Wei Zhai, Qing Ai, Jinkui Feng, Lin Zhang, Pengchao Si, and Lijie Ci. 2018. "Aluminum/Graphene Composites with Enhanced Heat-Dissipation Properties by in-Situ Reduction of Graphene Oxide on Aluminum Particles." *Journal of Alloys and Compounds* 748 (June): 854–60. doi:10.1016/j.jallcom.2018.03.237.

Zhang, Y. Y., Y. Cheng, Q. X. Pei, C. M. Wang, and Y. Xiang. 2012. "Thermal Conductivity of Defective Graphene." *Physics Letters, Section A: General, Atomic and Solid State Physics* 376 (47–48). North-Holland: 3668–72.

doi:10.1016/j.physleta.2012.10.048.

Zhang, Ya Fei, Dong Han, Yun Hong Zhao, and Shu Lin Bai. 2016. “High-Performance Thermal Interface Materials Consisting of Vertically Aligned Graphene Film and Polymer.” *Carbon* 109 (November). Elsevier Ltd: 552–57. doi:10.1016/j.carbon.2016.08.051.

Zheng, Zaihang, Yan Liu, Yuan Bai, Jijia Zhang, Zhiwu Han, and Luquan Ren. 2016. “Fabrication of Biomimetic Hydrophobic Patterned Graphene Surface with Ecofriendly Anti-Corrosion Properties for Al Alloy.” *Colloids and Surfaces A: Physicochemical and Engineering Aspects* 500 (July): 64–71. doi:10.1016/j.colsurfa.2016.04.008.

Zhou, Ya, Benjamin Anglin, and Alejandro Strachan. 2007. “Phonon Thermal Conductivity in Nanolaminated Composite Metals via Molecular Dynamics.” *Journal of Chemical Physics* 127 (18): 184702. doi:10.1063/1.2802366.

Zhou, Yu, Wu Gui Jiang, Xi Qiao Feng, Duo Sheng Li, Qing Hua Qin, and Xiao Bo Liu. 2019. “In-Plane Compressive Behavior of Graphene-Coated Aluminum Nano-Honeycombs.” *Computational Materials Science* 156 (January). Elsevier B.V.: 396–403. doi:10.1016/j.commatsci.2018.10.011.